TRANSPORTATION RESEARCH BOARD
NATIONAL RESEARCH COUNCIL

# IDEA

***Innovations Deserving Exploratory Analysis Project***

***NATIONAL COOPERATIVE HIGHWAY RESEARCH PROGRAM***

*Report of Investigation*

# IDEA PROJECT FINAL REPORT
# Contract NCHRP-34

**IDEA Program**
**Transportation Research Board**
**National Research Council**

**August, 1997**

THE HIGHWAY GUARDRAIL INFRASTRUCTURE:
SAFER TERMINAL DESIGN

*Prepared by:*
James F. Wilson and Nayer A. El-Esnawy
Department of Civil and Environmental Engineering
Duke University

**INNOVATIONS DESERVING EXPLORATORY ANALYSIS (IDEA) PROGRAMS**
**MANAGED BY THE TRANSPORTATION RESEARCH BOARD (TRB)**

This NCHRP-IDEA investigation was completed as part of the National Cooperative Highway Research Program (NCHRP). The NCHRP-IDEA program is one of the four IDEA programs managed by the Transportation Research Board (TRB) to foster innovations in highway and intermodal surface transportation systems. The other three IDEA program areas are Transit-IDEA, which focuses on products and results for transit practice, in support of the Transit Cooperative Research Program (TCRP), Safety-IDEA, which focuses on motor carrier safety practice, in support of the Federal Motor Carrier Safety Administration and Federal Railroad Administration, and High Speed Rail-IDEA (HSR), which focuses on products and results for high speed rail practice, in support of the Federal Railroad Administration. The four IDEA program areas are integrated to promote the development and testing of nontraditional and innovative concepts, methods, and technologies for surface transportation systems.

For information on the IDEA Program contact IDEA Program, Transportation Research Board, 500 5th Street, N.W., Washington, D.C. 20001 (phone: 202/334-1461, fax: 202/334-3471, http://www.nationalacademies.org/trb/idea)

# TABLE OF CONTENTS

## EXECUTIVE SUMMARY

Using the governing equations of the plastic failure load analysis discussed herein, three retrofit designs were developed to interface with present-day highway guardrail BCT systems. These retrofit designs have reduced buckling strength and other favorable design features. They are initially curved away from the direction of traffic flow, have corrugated sections that interface with highway guardrail BCT systems, and are flared width-wise and tapered depth-wise towards the impacted end. They are also inexpensive, easy to install, and do not require a different cable-release mechanism or additional terminal hardware. This general type of terminal structure is illustrated in Fig. 1.

The reduced buckling strength and flared ends of the retrofit designs reduce the potential of the highway guardrail terminals penetrating errant vehicles upon end impacts. Also, the potential for yaw motion of the errant vehicle upon impact is decreased and the potential for vehicle roll over is reduced, when compared to highway guardrail turned-down terminal designs. The flared profile of the retrofit designs provides a broad area of contact with the vehicle. As a result, the terminal-vehicle contact stresses are minimized. The flared profile also minimizes snagging that may occur between errant vehicles and guardrail posts. The key design feature that makes these designs so effective is that gross plastic failure occurs not at the interface with the existing guardrail, but in the middle third of the terminal.

An experimental program was carried out on two types of half-scale models that were based on the general static plastic failure analysis of flared, curved, corrugated terminals. The static experiments showed that plastic buckling did occur at the third point from the clamped ends, as predicted by static theory. Low speed crash tests were also performed on the half-scale models in which Duke University's test car, traveling at about 5 mph, impacted the models head-on. These test results showed that plastic failure occurred at about the two-thirds point from the fixed end. A failure model for such impacts has yet to be formulated, and this would be a topic of future work. Scaling laws are discussed herein, and the use of the present analysis and experimental data for full-scale applications is discussed.

The main objectives of this first year study were achieved, which were: to formulate a failure theory, to use this theory to design of flared, curved guardrail terminals that would not penetrate through vehicles that impacted them, and to design and test scale models to show proof of concept. Future work would involve the formulation of a dynamic impact failure theory together with complementary experiments on full-scale terminals with the present design characteristics. These new terminals would act efficiently when impacted with vehicles of different sizes and coming from both the head-on and the near head-on directions.

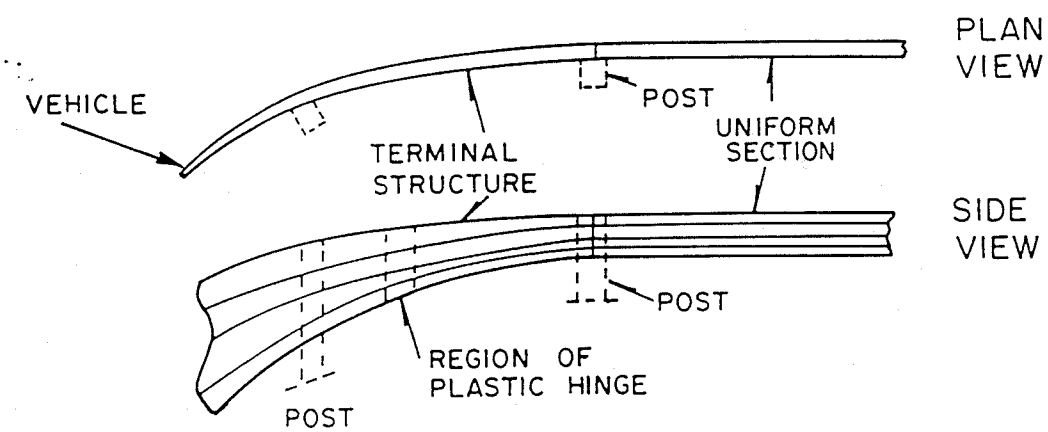


FIGURE 1 A typical new-concept terminal structure designed to avoid vehicle penetration.

## PLASTIC FAILURE LOAD ANALYSIS

A theoretical treatment based on the plastic hinge technique is developed to determine the static plastic collapse (gross plastic failure loads and failure locations) for a class of cantilevered beams that are initially curved and tapered. The beams are subjected to end loads, where shallow angles of the end loads are considered. The cross sections of the beams are thin-walled corrugated sections that interface with present-day guardrail Breakaway Cable Terminal (BCT) systems. Accordingly, the proposed theoretical treatment can be applied to future terminal retrofit designs for highway guardrail systems. The equations governing the proposed treatment are expressed in non-dimensional form, where small elastic displacements of the beam are considered. These equations are then used to investigate the effects of the following parameters on the static plastic collapse: the angle of the end load, the initial transverse end displacement, and the taper profile of the beam. The effect of the change of beam geometry during elastic loading on the static plastic collapse load is also investigated.

## INTRODUCTION

Tapered structural members such as beams and columns are widely used in various engineering applications. They have, therefore, been the subject of numerous investigations. Examples in the open literature include the works of Dinnik (1932), Timoshenko and Gere (1961), Ermopoulos (1986), William and Aston (1989), and Siginer (1992). These investigators discussed the elastic buckling loads for axially loaded tapered beams, considering several types of cross sections, end fixities, and taper profiles. Karabalis and Besko (1982) investigated the static, dynamic, and stability behavior of linear elastic plane structures consisting of tapered beams, and included a comprehensive survey of the related literature.

The elastic buckling loads of end-loaded, tapered, cantilevered steel beams having idealized thin-walled corrugated sections were discussed by Wilson and Strong (1997), who included the effects of the initial beam curvatures. One important application of tapered beams having initial curvatures is terminal designs for present-day highway guardrail systems. The ideal guardrail terminal design has several attributes: it is an energy absorber when impacted by an errant vehicle; it has sufficient strength to deflect an errant vehicle back to its travel lane; and it buckles sufficiently so that it does not penetrate an errant vehicle upon end impact. Guardrail terminal designs are constructed from galvanized steel beams that have thin-walled corrugated sections. These steel beams usually have moderate slenderness ratios and can, therefore, fail due to plastic deformations even before the elastic buckling loads are reached. If the guardrail terminal design is a tapered beam, then plastic deformations can develop at any section along the beam length. The section where plastic deformations develop and the corresponding gross plastic failure load will depend on the initial curvature, taper profile, and stiffness of the beam, as well as on the angle of impact of the errant vehicle.

Herein, a theoretical treatment is presented to determine the static plastic collapse load and collapse location for a class of end-loaded, initially curved, corrugated, tapered, cantilevered steel beams. This theoretical treatment is based on the plastic hinge technique (Horne, 1979). Models based on the plastic hinge technique have been commonly used to study structural collapse and vehicle crash simulations. These plastic hinge models provide favorable results for structural members made of ductile materials such as steel. They also require less computational effort and are relatively simple compared to finite element models (Nikravesh and Chung, 1984; Maruthayappan and Lankarani, 1994).

The analysis herein targets present-day guardrail Breakaway Cable Terminal (BCT) systems commonly installed on highways in the United States. As a result of their high buckling strength, present-day guardrail BCT systems often perform inadequately in case of nearly head-on or shallow impacts (Pigman and Agent, 1988). They sometimes penetrate impacting vehicles, especially present-day small, light-weight passenger vehicles. Accordingly, the cross sections of the cantilevered beams are thin-walled corrugated sections that interface with present-day highway guardrail BCT systems. Also, shallow angles for the end loads of the beam are considered. For design purposes, a favorable location for plastic deformations of these tapered, cantilevered beams is away from the fixed end, which in turn reduces the buckling strength

of the beam. These initially curved, corrugated, tapered, cantilevered steel beams having reduced buckling strength can serve as models for future terminal retrofit designs for highway guardrail BCT systems.

## BEAM CHARACTERISTICS

Consider the cantilevered steel beam shown in Fig. 2(a), where $x$ is the longitudinal axis whose origin is the centroid of the beam section located at the fixed end. The beam is of length $L_b$ and is subjected to an end load $F$ inclined at angle $\beta$ to the $x$-axis. The unloaded beam is initially curved, where the initial configuration $y_o(x)$ can be either a parabolic arc or a circular arc with small initial curvatures, or

$$y_o(x) = d_b \left( \frac{x}{L_b} \right)^2 \tag{1}$$

where $d_b$ is the initial end displacement of the beam relative to the fixed end directed along the transverse $y$-axis. The beam has the cross section shown in Fig. 1(b), referred to as the W-section. This W-section has one plane of symmetry

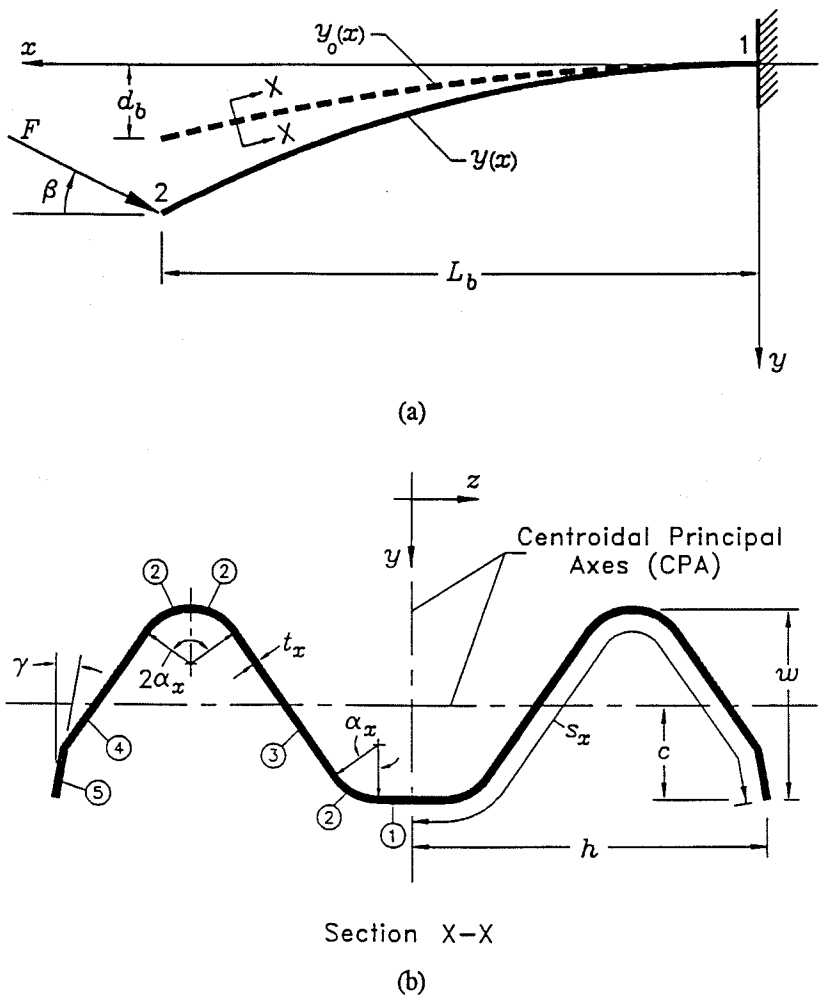


**FIGURE 2 Model of the initially curved, cantilevered beam: (a) geometric characteristics and end load in the $xy$-plane, (b) typical full W-section in the $yz$-plane.**

through the transverse $y$-axis (the $y$-axis is the centroidal principal symmetry-axis of the W-section). It comprises straight segments (denoted by 1,3,4, and 5) and circular segments (denoted by 2), where the straight segments are tangent to the adjacent circular segments. The W-section is defined herein by the following parameters: the thickness $t_x$, the arc length $s_x$, and the angle $\alpha_x$ of the corrugation. In terms of these parameters, some area properties of the W-section, at a distance $x$ along the beam length, are as follows:

$$w(x) = s_x \, G_1(\alpha_x) \tag{2a}$$

$$A(x) = 2 \, s_x \, t_x \tag{2b}$$

$$c(x) = s_x \, G_2(\alpha_x) \tag{2c}$$

$$I(x) = \frac{1}{12} \, s_x^3 \, t_x \, G_3(\alpha_x) + \frac{\eta_1}{6} \, s_x \, t_x^3 \tag{2d}$$

$$h(x) = \left( \eta_1 + \eta_5 \, (\eta_3 + \eta_4) \cos\alpha_x \cos\gamma(x) + 3 \, \eta_2 \, \frac{\sin\alpha_x}{\alpha_x} \right) s_x \tag{2e}$$

$$\gamma(x) = \arcsin\left( \frac{1}{2 \, \eta_5} \left[ G_1(\alpha_x) + (\eta_3 - 2 \, \eta_4) \sin\alpha_x \right] \right) \tag{2f}$$

where $w$ is the corrugation depth, $A$ is the cross sectional area, $c$ is the location of the centroidal principal asymmetry-axis which is parallel to the transverse $z$-axis, $I$ is the second area moment about the centroidal principal asymmetry-axis, $h$ is half the corrugation width, and $\gamma$ is the angle of the straight segment or item 5 of the W-section (see Figure 1). In equations (2), $G_j(\alpha_x)$, $j$=1,2,..,5, are functions of the corrugation angle, which are given in Appendix I, and $\eta_i$, $i$=1,2,..,5, are ratios of the length or arc length of the $i$th straight or circular segment to $s_x$.

The cantilevered beam is tapered along its length such that the ratios $\eta_i$ are constant, and the thickness of the corrugation is constant ($t_x$=$t$). Meanwhile, the arc length and the angle of the corrugation are considered to vary linearly along the length of the beam, or

$$s_x = s_1 + \frac{(s_2 - s_1)}{L_b} \, x \tag{3}$$

$$\alpha_x = \alpha_1 + \frac{(\alpha_2 - \alpha_1)}{L_b} \, x \tag{4}$$

In equations (3) and (4), $s_1$ and $\alpha_1$ are the arc length and the angle of the corrugation at the fixed end, respectively, while $s_2$ and $\alpha_2$ are those parameters at the free end of the beam. The variation of $s_x$ reflects the form of the flat steel sheet used for manufacturing the W-section of the beam. Accordingly, the linear variation of the arc length of the corrugation given by equation (4) indicates that this flat steel sheet has an initial trapezoidal form ($s_2 \neq s_1$) or rectangular form ($s_2$=$s_1$).

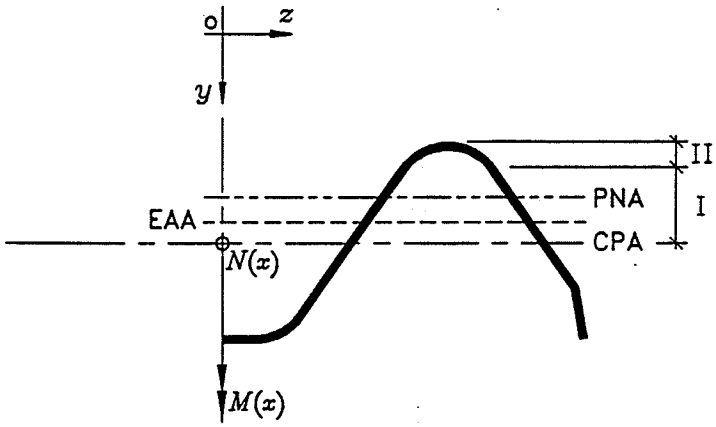


**FIGURE 3 Schematic of half W-section of the beam model showing the CPA, EAA, and PNA as well as the normal compressive force and bending moment due to end load.**

## THEORETICAL TREATMENT

Consider now the case of bending in the plane of symmetry of the W-section of the beam, i.e., bending around the centroidal principal asymmetry-axis (CPA) as shown in Fig. 2. A favorable mathematical model for the behavior of the steel beam beyond its yield stress $\sigma_y$ is the perfectly-plastic model. Accordingly, the static plastic collapse of the beam can be reasonably determined using the plastic hinge technique. In this technique, plastic hinges occur at sections that have become fully plastic due to bending moments of applied loads. Each plastic hinge has a constant moment of resistance, which is the full plastic moment $M_{FP}$ of the corresponding section. When sufficient plastic hinges have formed to develop a kinematically admissible collapse mechanism for the structural member, gross plastic failure is considered to occur. One plastic hinge is, therefore, required for the static plastic collapse of the cantilevered beam shown in Fig.1.

The full plastic moment of the W-section is reduced by both the normal compressive force $N(x)$ and the shear force of the end load of the cantilevered beam. The effect of the shear force may, however, be neglected in case of shallow angles of the end load, since the shear force is relatively small compared to the maximum shear load carrying capacity of the W-section (Horne and Morris, 1982). In this case, considering only the effect of $N(x)$, the reduced plastic moment $M_{RP}$ of the W-section, at a distance $x$ along the beam length, determined about the CPA is given by

$$M_{RP}(x) = M_{FP}(x) - k_1 \left[ f(\alpha_x, \lambda(x)) + k_2 \lambda(x) \left( G_4(\alpha_x) - G_2(\alpha_x) \right) \right] N_y(x)\, s_x \tag{5a}$$

where

$$M_{FP}(x) = Z_{FP}(x)\, \sigma_y \tag{5b}$$

$$\lambda(x) = \frac{N(x)}{N_y(x)} \tag{5c}$$

In equation (5a), the term operated on by $k_1$ represents the effect of the normal compressive force $N(x)$, where $k_1$ and $k_2$ are indicators that have values of 0 or 1. $Z_{FP}$ is the plastic modulus of the W-section considering no normal

compressive force. This plastic modulus is determined by taking the first moment of area about the equal area axis (EAA, the axis which divides the W-section into two equal areas) regarding the moment on either side of the EAA to be positive. That is

$$Z_{FP}(x) = 2\ t\ s_x^2\ G_5(\alpha_x) \tag{6}$$

$\lambda(x)$ defined by equation (5c) is referred to as the squash load ratio, where $N_y(x)$ is the maximum normal load carrying capacity of the W-section for the case of no bending moment (the squash load), or

$$N_y(x) = A(x)\ \sigma_y = 2\ t\ s_x\ \sigma_y \tag{7}$$

The function $f(\alpha_x, \lambda(x))$ in equation (5a) depends on the location of the plastic neutral axis (PNA, the neutral axis for a fully plastic W-section). In the absence of $N(x)$, the PNA and the EAA are coincident. In the presence of $N(x)$, the PNA moves in the negative $y$-direction (see Fig. 2). If the squash load ratio is $\lambda(x) \leq (1-4\ \eta_2)$, then the PNA will lie across the straight segments denoted by 3 and 4 (Region I in Fig. 2), otherwise it will lie across the top circular segments denoted by 2 (Region II). For the former case,

$$f(\alpha_x, \lambda(x)) = \frac{1}{8}\ (\lambda(x))^2\ \sin\alpha_x \tag{8}$$

while for the latter case,

$$\begin{aligned} f(\alpha_x, \lambda(x)) = {} & \frac{1}{8}\ (1-4\eta_2)^2 \sin\alpha_x - \frac{4\ \eta_2^2}{\alpha_x^2}\left(\sin\left[\frac{\alpha_x}{4\eta_2}(1-\lambda(x))\right] - \sin\alpha_x\right) \\ & - (1-4\ \eta_2 - \lambda(x))\left(G_1(\alpha_x) - G_4(\alpha_x) - \frac{\eta_2}{\alpha_x}\right) \end{aligned} \tag{9}$$

The term operated on by $k_2$ in equation (5a) is a result of the difference between the location of the EAA and the location of the CPA because of the monosymmetery of the W-section. If the effect of this difference between the CPA and the EAA is neglected, then $k_2=0$; if the effect of $N(x)$ is neglected, then $k_1=0$ ($k_2=0$ as well); otherwise $k_1=k_2=1$. For a typical highway guardrail W-section, the difference between the CPA and the EAA is negligible. Therefore, $k_2=0$ is assumed hereafter.

The end load $F$ of the cantilevered beam is considered to lie in the plane of the centroidal axes of the W-section. Shallow angles of the end load $\beta$ are considered, where $\beta=0$ to 15 degrees. Elastic deformations of the beam due to $F$ are considered small and changes of $L_b$ and $\beta$ during loading are, therefore, neglected. In this case, for small initial curvatures, the normal compressive force and the bending moment, at a distance $x$ along the beam length, due to $F$ are respectively given by

$$N(x) = \left[\cos\beta - \frac{dy(x)}{dx}\sin\beta\right] F \tag{10}$$

$$M(x) = \left[(L_b - x)\sin\beta + (y_2 - y(x))\cos\beta\right] F \tag{11}$$

where $y(x)$ and $y_2$ are the elastic transverse displacement curve and end displacement of the loaded beam, respectively.

Neglect now the effect of the spread of the plastic zone on the beam deformations that follow the first yield of the W-section until the section becomes fully plastic. Then, based on the plastic hinge technique, a plastic hinge occurs at the W-section where the bending moment due to $F$ given by equation (11) approaches the plastic moment given by equation (5a). The end load at which the plastic hinge occurs is considered the gross plastic failure load $F_{GP}$ (the static plastic collapse load) of the initially curved, cantilevered beam. For a uniform cantilevered beam, the plastic hinge occurs at the section located at the fixed end. For a tapered cantilevered beam, the plastic hinge can occur at any section along the beam length, especially in case of shallow angles $\beta$ of the end load. In this latter case, considering the effect of $N(x)$, the reduced plastic moment curve of the beam forms an envelope which is tangent to the bending moment curve corresponding to the gross plastic failure load at the location of the plastic hinge $x_p$, or

$$M(x) = M_{RP}(x) \qquad \text{at} \quad x = x_p\,, \qquad \text{and} \quad F = F_{GP} \tag{12}$$

$$\frac{dM(x)}{dx} = \frac{dM_{RP}(x)}{dx} \qquad \text{at} \quad x = x_p\,, \qquad \text{and} \quad F = F_{GP} \tag{13}$$

Equations (12) and (13) can be used to determine the gross plastic failure load of an end-loaded, initially curved, tapered, cantilevered steel beam, as well as the corresponding location of the plastic hinge. If $x_p$ obtained from solving these two equations, lies outside the feasible range, $x_p$=0 to $L_b$, then the feasible solution is that the plastic hinge occurs at the fixed end, $x_p$=0. In this case, only equation (12) governs the determination of the gross plastic failure load $F_{GP}$.

Application of equations (12) and (13) is now illustrated for the case in which the PNA lies in Region I (see Fig. 3), where the function $f(\alpha_x, \lambda(x))$ in equation (5a) is given by equation (8). For a typical W-section for highway guardrail systems, the term $(1-4\eta_2)\approx 0.6$ and, considering $\sigma_y$=345 MN/m$^2$, the maximum normal load carrying capacity $N_y(x)$ is about 0.46 MN, which is equivalent to a vehicle of mass 2200 kg having a constant deceleration of 21$g$, where $g$ is the acceleration due to gravity. Accordingly, the case of $\lambda(x) \leq 0.6$ ($N(x) \leq 60\%$ of $N_y(x)$) accommodates a practical range for the beam end loads. For this case, the results of applying equations (12) and (13) were expressed in non-dimensional form using the following notation: a bar denotes a non-dimensional parameter, and a subscript $p$ denotes a parameter evaluated at the location of the plastic hinge. Thus, the result of applying equation (12) is

$$\bar{s}_p^2\, G_5(\alpha_p) - \frac{k_1}{8}\, \bar{F}_{GP}^2 \bar{N}_p^2 \sin\alpha_p - \bar{F}_{GP}\, \bar{l}\left[(1-\bar{x}_p)\sin\beta + (\bar{y}_2 - \bar{y}_p)\cos\beta\right] = 0 \tag{14}$$

while the result of applying equation (13) is

$$\begin{aligned} &\bar{s}_p^2\,(\alpha_2 - \alpha_1)\,\frac{dG_5(\alpha_x)}{d\alpha_x}\Big|_{\alpha_x=\alpha_p} + 2\,\bar{s}_p\,(\bar{s}_2 - 1)\,G_5(\alpha_p) \\ &- \frac{k_1}{8}\,\bar{F}_{GP}^2 \bar{N}_p \left(\bar{N}_p\,(\alpha_2 - \alpha_1)\cos\alpha_p + 2\,\frac{d^2\bar{y}}{d\bar{x}^2}\Big|_{\bar{x}=\bar{x}_p}\sin\beta\,\sin\alpha_p\right) \\ &\qquad + \bar{F}_{GP}\,\bar{l}\left(\sin\beta + \frac{d\bar{y}}{d\bar{x}}\Big|_{\bar{x}=\bar{x}_p}\cos\beta\right) = 0 \end{aligned} \tag{15}$$

where

$$\bar{x} = \frac{x}{L_b}\,, \qquad \bar{x}_p = \frac{x_p}{L_b} \tag{16}$$

$$\bar{y} = \frac{y(x)}{L_b}\,, \qquad \bar{y}_p = \frac{y(x_p)}{L_b}\,, \qquad \bar{y}_2 = \frac{y(L_b)}{L_b} \tag{17}$$

$$\bar{F}_{GP} = \frac{F_{GP}}{2\, t\, s_1\, \sigma_Y}\,, \qquad \bar{l} = \frac{L_b}{s_1} \tag{18}$$

$$\alpha_p = \alpha_1 + (\alpha_2 - \alpha_1)\, \bar{x}_p \tag{19}$$

$$\bar{s}_p = \frac{s_p}{s_1} = 1 + (\bar{s}_2 - 1)\, \bar{x}_p\,, \qquad \bar{s}_2 = \frac{s_2}{s_1} \tag{20}$$

$$\bar{N}_p = \cos\beta - \frac{d\bar{y}}{d\bar{x}}\Big|_{\bar{x}=\bar{x}_p} \sin\beta \tag{21}$$

Equations (14) and (15) are nonlinear and a numerical scheme such as Newton-Raphson may be used to solve these equations for both the gross plastic failure load $\bar{F}_{GP}$ and the corresponding location of the plastic hinge $\bar{x}_p$. These two equations were solved herein using the Newton-Raphson scheme implemented in *Mathematica* (Wolfram, 1993).

If the effect of the normal compressive force in equations (14) and (15) is neglected ($k_1$ =0), then an upper bound on the gross plastic failure load $\bar{F}^u_{GP}$ can be determined. In this case, equation (14) gives

$$\bar{F}^u_{GP} = \frac{\bar{s}_p^2\, G_5(\alpha_p)}{\bar{l}\,[\,(1-\bar{x}_p)\,\sin\beta + (\bar{y}_2 - \bar{y}_p)\,\cos\beta\,]} \tag{22}$$

Substituting equation (22) into equation (15) yields

$$\bar{s}_p^2\,(\alpha_2 - \alpha_1)\,\frac{dG_5(\alpha_x)}{d\alpha_x}\Big|_{\alpha_x=\alpha_p} + 2\,\bar{s}_p\,(\bar{s}_2 - 1)\,G_5(\alpha_p) + \frac{\bar{s}_p^2\, G_5(\alpha_p)\left(\sin\beta + \frac{d\bar{y}}{d\bar{x}}\Big|_{\bar{x}=\bar{x}_p}\cos\beta\right)}{[\,(1-\bar{x}_p)\sin\beta + (\bar{y}_2 - \bar{y}_p)\,\cos\beta\,]} = 0 \tag{23}$$

Equation (23) can be solved for $\bar{x}_p$, and this value is then substituted back into equation (22) to determine $\bar{F}^u_{GP}$.

As mentioned earlier, if solving equations (14) and (15) or equation (23) yields $\bar{x}_p$ outside the feasible range, $\bar{x}_p$ =0 to 1, then the feasible solution is $\bar{x}_p$ =0. In this case, the expected gross plastic failure load or its upper bound is governed by equation (14) or equation (22), respectively.

## PRACTICAL CONSIDERATIONS

The equations governing the proposed theoretical treatment, equations (14) and (15), involve the expected elastic curve of the transverse displacement of the loaded beam ($\bar{y}$, $\bar{y}_p$, $\bar{y}_2$). A closed form expression for this elastic curve is impractical to implement because of the change of the beam geometry during loading. Accordingly, some practical idealizations are considered.

The simplest idealization is to ignore the elasticity of the cantilevered beam by assuming that the beam behaves in a rigid perfectly-plastic manner. In this case, the transverse displacement curve of the beam before yielding, expressed in

non-dimensional form, is

$$\bar{y} = \frac{y_o(x)}{L_b} = \Delta_b \bar{x}^2 , \qquad \Delta_b = \frac{d_b}{L_b} \tag{24}$$

Accordingly, $\bar{y}_p = \Delta_b \bar{x}_p^2$ and $\bar{y}_2 = \Delta_b$. For this rigid perfectly-plastic case, $F_{GP}$ is always higher than the true static plastic collapse load of the beam.

Another idealization is to include an approximate elasticity by considering the linear elastic curve for the transverse displacement of a similar cantilevered beam having an approximate variation for the second area moment of the W-section $I_a(x)$ along the beam length. A commonly used form for the variation of the second area moment of a tapered beam member is a power law of $x$ (Timoshenko and Gere, 1961; Ermopoulos, 1986; Wilson and Strong, 1997; Al-Gahtani, 1996). A quadratic power law was used by Wilson and Strong (1997) to approximate the variation of the second area moment for their idealized thin-walled corrugated section. This power law for the beam in Fig. 2 is expressed as

$$I_a(x) = I_1 \left[ 1 - ( 1 - \sqrt{\kappa} ) \frac{x}{L_b} \right]^2 \tag{25}$$

where $\kappa$ is the taper ratio defined by

$$\kappa = \frac{I_2}{I_1} \tag{26}$$

and $I_1$ and $I_2$ are the exact values of the second area moments of the W-section of the beam at the fixed end and the free end, respectively.

A closed form expression for an approximate linear elastic curve for the transverse displacement of the loaded cantilevered beam $y_{la}(x)$ was derived based on the classical beam theory, or

$$E\, I_a(x) \left[ \frac{d^2 y_{la}(x)}{dx^2} - \frac{d^2 y_o(x)}{dx^2} \right] = \left[ (L_b - x) \sin\beta + ( d_b - y_o(x) ) \cos\beta \right] F \tag{27}$$

where $E$ is Young's modulus of the beam. This approximate linear elastic curve, expressed in non-dimensional form ($\bar{y}_{la} = y_{la}(x)/L_b$), is

$$\bar{y}_{la} = \Delta_b \bar{x}^2 + \bar{F}\bar{Q} \left[ g_1(\kappa, \beta, \Delta_b) - \frac{\Delta_b \bar{x} \cos\beta}{2\,(1 - \sqrt{\kappa})^2} \right] \bar{x} + \bar{F}\bar{Q} \left[ \frac{g_1(\kappa, \beta, \Delta_b)}{1 - \sqrt{\kappa}} - g_2(\kappa, \beta, \Delta_b)\, \bar{x} \right] \ln[1 - (1 - \sqrt{\kappa})\, \bar{x}] \tag{28}$$

where

$$\bar{F} = \frac{F}{2\, t\, s_1\, \sigma_y} , \qquad \bar{Q} = \frac{\pi^2\, t\, s_1\, \sigma_y}{2\, Q_{cr}} , \qquad Q_{cr} = \frac{\pi^2\, E\, I_1}{4\, L_b^2} \tag{29}$$

$$g_1(\kappa, \beta, \Delta_b) = \frac{(1-\kappa)\sin\beta + \Delta_b\,(2-\kappa+2\sqrt{\kappa})\cos\beta}{(1-\sqrt{\kappa})^3} \tag{30}$$

$$g_2(\kappa, \beta, \Delta_b) = \frac{(1-\sqrt{\kappa})\sin\beta + 2\,\Delta_b\cos\beta}{(1-\sqrt{\kappa})^3} \tag{31}$$

In equation (28), $\bar{F}$ is a non-dimensional parameter for the end load, and $\bar{Q}$ is a non-dimensional parameter reflecting the stiffness of the beam, where $Q_{cr}$ is the critical Euler buckling load for a uniform cantilevered beam where $I(x)=I_1$. In this linear elastic perfectly-plastic case, $\bar{y} = \bar{y}_{la}$, $\bar{y}_p = \bar{y}_{la}$ at $\bar{x} = \bar{x}_p$, and $\bar{y}_2 = \bar{y}_{la}$ at $\bar{x} = 1$. For this case, $F_{GP}$ is still higher than the true static plastic collapse load of the beam, since the effects of the change of beam geometry and the spread of the plastic zone during loading are not considered. However, $F_{GP}$ of this linear elastic perfectly-plastic case is lower than that of the rigid perfectly-plastic case.

## NUMERICAL RESULTS AND DISCUSSION

Consider an end-loaded, initially curved, tapered, corrugated, cantilevered steel beam having the following reference parameters: $L_b$=1.0 m, $d_b$=0.1 m, $E$=200 GN/m$^2$, $\sigma_y$=345 MN/m$^2$, t=0.003 m, $s_1$=0.2 m, $\alpha_1$=0.96, $s_2$=0.185 m, $\alpha_2$=0.35, $\eta_1$=0.059, $\eta_2$=0.094, $\eta_3$=0.313, $\eta_4$=0.254, and $\eta_5$=0.092. For this beam, the difference between the CPA and the EAA along the beam length is less than 1%. The difference between $I(x)$, equation (2d), and $I_a(x)$, equation (25), is shown in Fig. 4, where the maximum error is less than 4% when compared to $I(x)$. The exact linear deflection curve of the beam, $\delta y_l(x) = y_l(x) - y_o(x)$, where $y_l(x)$ was determined numerically using *Mathematica*, is shown in Fig. 5, for the cases $\beta$=0 and 15 degrees, together with the approximate linear deflection curve $\delta y_{la}(x)$, where $y_{la}(x)$ was determined by equation (28). The shown deflection curves are normalized with respect to $\delta y_r = \delta y_l(L_b)$ for $\beta$=15 degrees. The maximum error between the exact and approximate end deflection of the beam, for both cases of $\beta$, is less than 3% when compared to the exact end deflection.

Using the governing equations of the proposed theoretical treatment, equations (14) and (15), the effect of the angle of the end load $\beta$ on the expected gross plastic failure load $F_{GP}$ and the corresponding location of the plastic hinge $x_p$ is shown in Figs. 6(a) and (b), respectively. The results shown are those of the rigid perfectly-plastic case (R-case), the approximate linear elastic perfectly-plastic case (LE-case), and EPFRAME: a program for elastic perfectly-plastic analysis of plane frames (Lee and Goel, 1986). For this latter program, the tapered beam was discretized into 100 uniform beam elements, where the full plastic moment of each element, in the case of no normal compressive force ($k_1$=0), was calculated at the mid length of the element. The output of the EPFRAME includes the expected rigid plastic failure load and the corresponding location of the plastic hinge. As shown in Figs. 6(a) and (b), $F_{GP}$ and $x_p$ of the proposed theoretical treatment, for the R-case ($k_1$=0), are in very good agreement with those of EPFRAME. The small differences, especially for $x_p$, are due to the discretization of the beam model. The results shown in Fig. 6(a) are normalized with respect to $F_r = F_{GP}$ of the R-case considering $k_1$=0 and $\beta$=0.

Figure 6(a) shows that $F_{GP}$ decreases monotonically as $\beta$ increases. The influence of the normal compressive force on $F_{GP}$ for the R-case is small and decreases as $\beta$ increases. $F_{GP}$ for the LE-case is less than $F_{GP}$ for the R-case, as expected. The difference between $F_{GP}$ of the LE-case and the corresponding $F_{GP}$ of the R-case decreases as $\beta$ increases. This difference is less than 30% for $\beta$=0 when compared to the LE-case, while it is less than 17% for $\beta$=7 degrees and less than 10% for $\beta$=15 degrees.

The crush load ratio at the plastic hinge was $\lambda(x_p) \le (1-4\,\eta_2)$=62.4%. The application of equations (14) and (15) is valid. Therefore, the effect of the shear force on $F_{GP}$ is negligible.

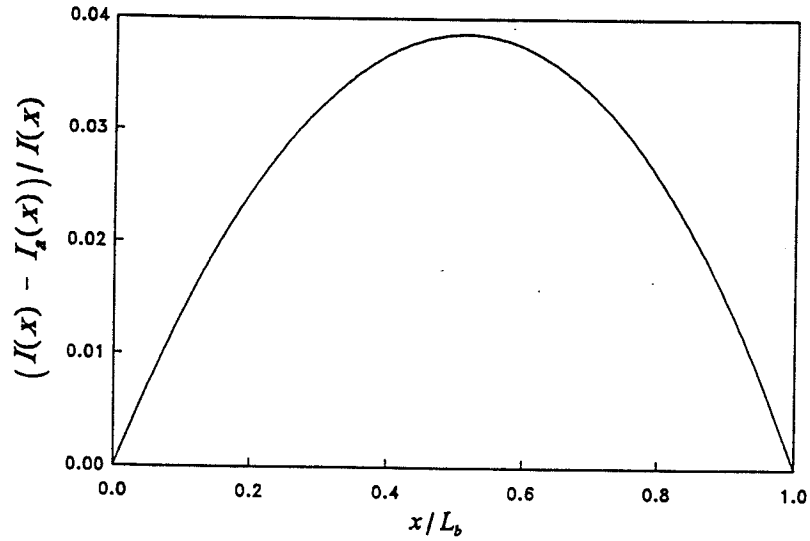


**FIGURE 4 Difference between exact and approximate second area moments along beam length.**

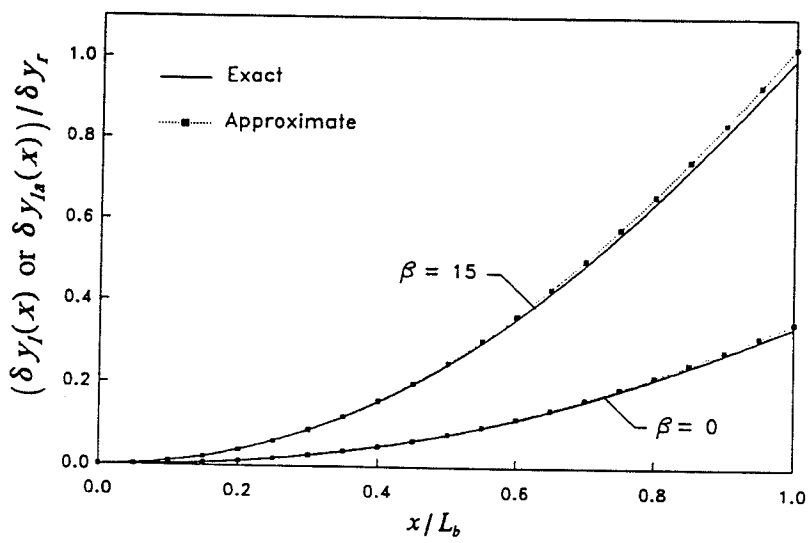


**FIGURE 5 Exact and approximate linear elastic deflection curves of beam for β=0 and 15 degrees.**

Figure 6(b) shows that the relation between β and $x_p$ is almost linear for the R-case as well as for the LE-case. As β increases, $x_p$ moves towards the fixed end. $x_p$ for the R-case approaches the fixed end at a smaller β compared to the LE-case.

The effect of the initial transverse end displacement of the beam $d_b$ on $F_{GP}$ and $x_p$ for the LE-case ($k_l$ =1) is respectively shown in Figs. 7(a) and (b), for the cases β=0, 1, 5, 10, and 15 degrees. Figure 7(a) shows that $F_{GP}$ decreases as $d_b$ increases, as expected. For very small β-angles, the decrease in $F_{GP}$ is relatively larger than that for moderate and large β-angles in the shallow range. For β=0, the decrease in $F_{GP}$ for $d_b$ =20% of $L_b$ is about 80% when compared to $d_b$ =2% of $L_b$, while this decrease is about 37% for β=15 degrees. For large β-angles, the contribution

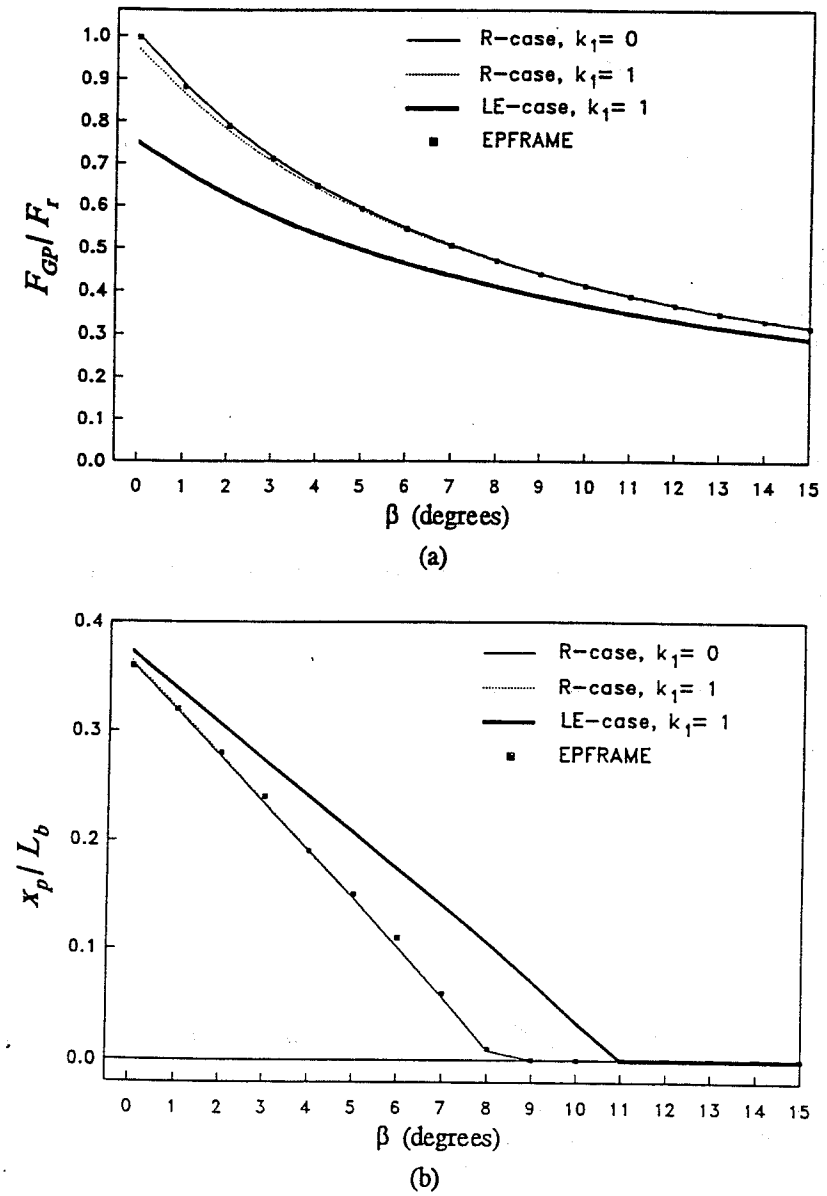


**FIGURE 6 Effect of angle of end load on: (a) plastic failure load, (b) plastic hinge location.**

of the transverse force component of the end load to $M(x)$ is larger than that of the longitudinal force component and the effect of $d_b$ is, therefore, reduced.

Figure 7(b) shows that, except for $\beta = 0$, $x_p$ moves away from the fixed end as $d_b$ increases. $x_p$ is, however, slightly affected by $d_b$ for small β-angles. For moderate and large β-angles, the plastic hinge occurs away from the fixed end ($x_p$>0) if $d_b$ exceeds a critical value. This critical value is, for example, 2% of $L_b$ for $\beta = 5$ degrees and 14% of $L_b$ for $\beta = 15$ degrees. As $d_b$ increases beyond the critical value, the effect of $d_b$ on $x_p$ is initially significant and then decreases.

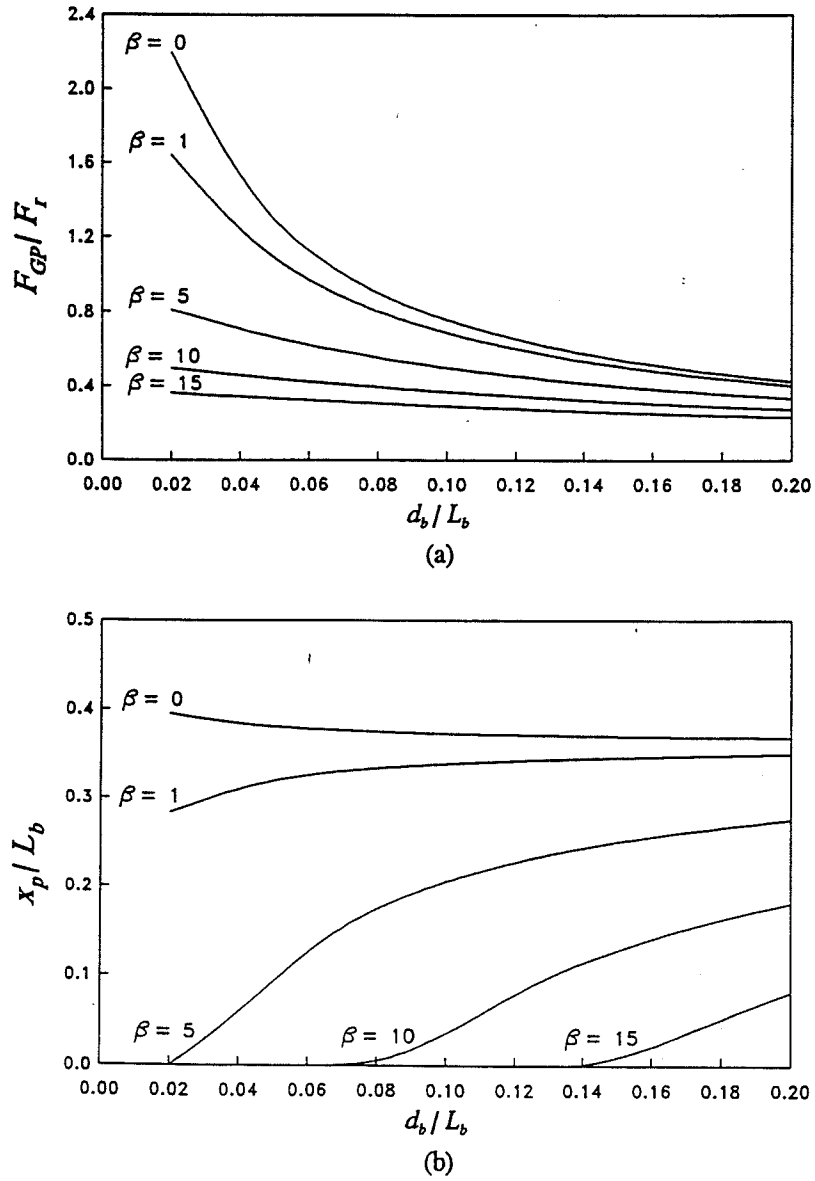


**FIGURE 7 Effect of initial end displacement of beam on: (a) plastic failure load, (b) plastic hinge location.**

The effect of the angle of the corrugation at the free end $\alpha_2$ on $F_{GP}$ and $x_p$ for the LE-case ($k_1$ =1) is respectively shown in Figs. 8(a) and (b), for the cases β=0, 1, 5, 10, and 15 degrees. Figure 8(a) shows that $F_{GP}$ decreases as $\alpha_2$ decreases, as expected, since the full plastic moment of the W-section of the beam decreases. For very small β-angles, the decrease in $F_{GP}$ is larger than that for moderate and large β-angles in the shallow range. For β=0, the decrease in $F_{GP}$ for $\alpha_2$ =0.14 is about 27% when compared to $\alpha_2$ =0.70, while this decrease is about 6% for β=15 degrees.

For $\alpha_2$ =0.14 the taper ratio κ is 0.023 and the difference between the exact and approximate second area moment is less than 7%, while these values for $\alpha_2$ =0.70 are 0.482 and 0.5%, respectively. For very small taper ratios, usually less than 0.1, the assumption of small elastic deformations may not be adequate as the beam undergoes relatively large elastic deformations as compared to a beam with a larger taper ratio.

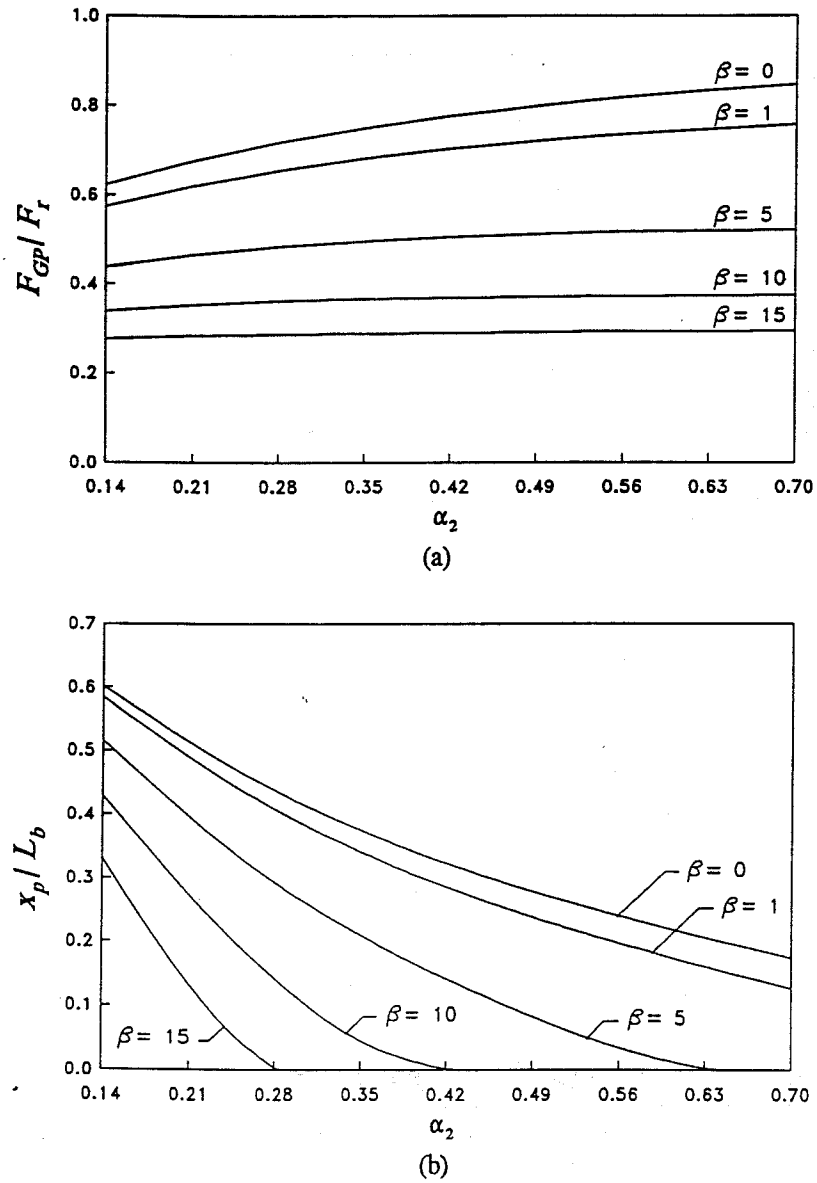


**FIGURE 8 Effect of angle of corrugation on: (a) plastic failure load, (b) plastic hinge.**

Figure 8(b) shows that $x_p$ moves away from the fixed end as $\alpha_2$ decreases. The plastic hinge occurs away from the fixed end ($x_p$>0) if $\alpha_2$ is less than a critical value. This critical value is, for example, 0.63 for $\beta$ = 5 degrees and 0.28 for $\beta$ = 15 degrees. As $\alpha_2$ decreases below the critical value, the effect of $\alpha_2$ on $x_p$ is initially small and then increases significantly, especially for large $\beta$-angles.

## EFFECT OF CHANGE OF BEAM GEOMETRY

Consider now how the change of beam geometry during elastic loading affects $F_{GP}$ . The gross plastic failure load (the static plastic collapse load) of this case was determined herein following Horne (1979), who considered the static plastic collapse load of an eccentrically loaded column having a rectangular cross section. Horne determined the static

plastic collapse load of the column, considering the effect of the change of geometry during loading, as the point of intersection of the elastic buckling curve and the rigid perfectly-plastic mechanism curve of the column.

The elastic buckling curve was determined herein following Wilson and Strong (1997), where the reference parameters in Section 5 and $I_a(x)$ in equation (25) were employed. Wilson and Strong presented the differential equation governing the elastic deflection of an initially curved, tapered, cantilevered beam, and then transformed that equation to a differential equation with constant coefficients. Herein, this transformed differential equation was numerically solved using *Mathematica* to obtain the elastic buckling curve of the beam ($F_b$ versus $y_{2b}$).

The rigid perfectly-plastic mechanism curve was determined considering the mechanism shown in Fig. 9. For small plastic hinge rotations, $M_{FP}(x)$ at the plastic hinge and $\beta$ were considered constant during the mechanism. In this case, neglecting the effect of $N(x)$, the rigid perfectly-plastic mechanism curve ($F_m$ versus $y_{2m}$) is

$$F_m = \frac{M_{FP}(x_p)}{(y_{2m} - y_o(x_p))\cos\beta + \sin\beta\sqrt{(L_b - x_p)^2 + (d_b - y_o(x_p))^2 - (y_{2m} - y_o(x_p))^2}} \tag{32}$$

where $M_{FP}(x)$ is given by equation (5b) and $y_o(x)$ is given by equation (1).

The elastic buckling curve and the rigid perfectly-plastic mechanism curve are shown in Fig. 10, for the cases $\beta = 0$ and 15 degrees. The point of intersection of these two curves is $F_{GP}$, where the effect of the change of beam geometry during elastic loading is considered (EBM-case). This $F_{GP}$ of the EBM-case is still higher than, but close to, the true static plastic collapse load of the beam as the spread of the plastic zone is ignored. As shown in Fig. 10, the elastic buckling curves rise asymptotically to the expected elastic buckling loads. These elastic buckling loads, for both cases of $\beta$, are higher than $F_{GP}$ of the EBM-case. Therefore, the beam fails due to the development of plastic deformations.

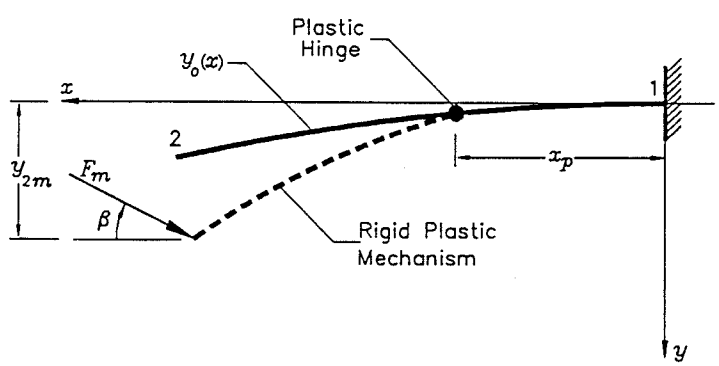


**FIGURE 9 Rigid perfectly-plastic mechanism of initially curved, cantilevered beam.**

$F_{GP}$ of the EBM-case for different $\beta$-angles are shown in Fig. 11, together with those of the LE-case. The loads at first yield of the W-sections located at the plastic hinges $F_y$ are also shown for the rigid case (YR-case) and for the approximate linear elastic case (YLE-case). These yield loads are determined based on the classical beam theory, where the effect of the compressive normal force is included.

As shown in Fig. 11, the effect of the change of beam geometry during loading on $F_{GP}$ is relatively high for small $\beta$-angles. For moderate and large $\beta$-angles, $F_{GP}$ of the EBM-case is very close to that of the LE-case. The difference

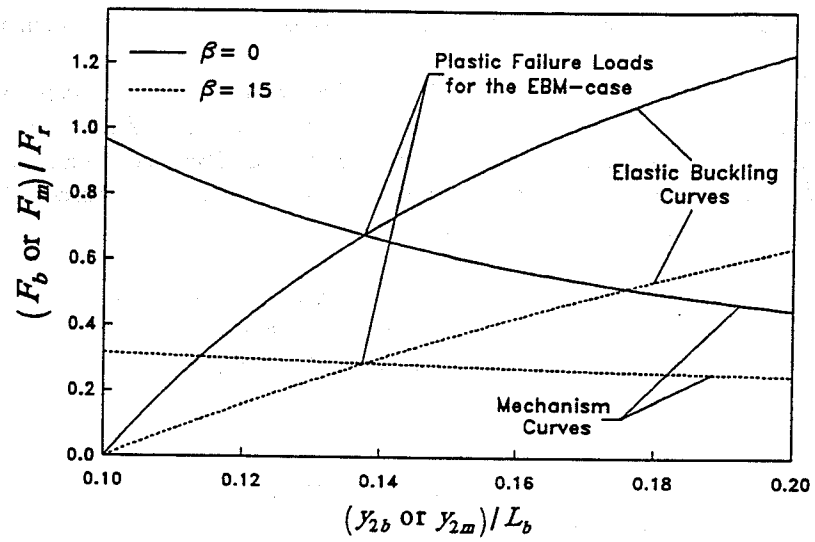


**FIGURE 10 Elastic buckling and rigid perfectly-plastic mechanism curves for β=0 and 15 degrees.**

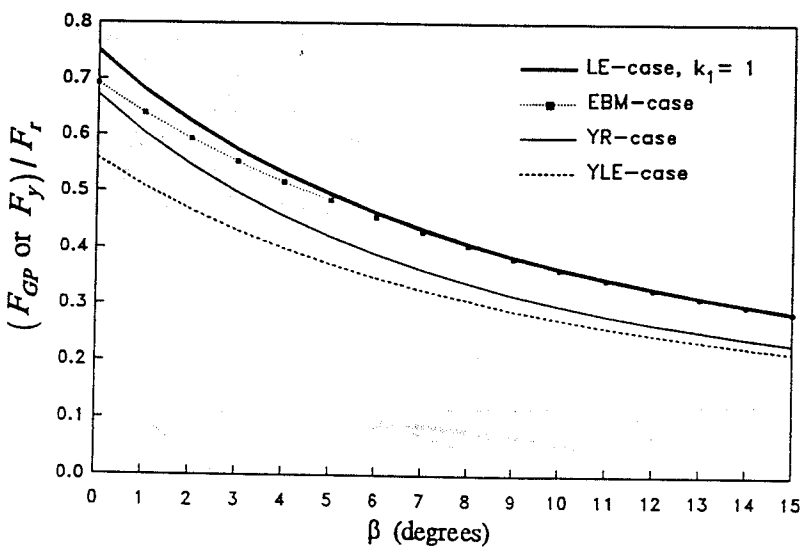


**FIGURE 11 Plastic failure loads, considering change of beam geometry during elastic loading, for different angles of end load of beam.**

in $F_{GP}$ between these two cases is less than 8% for β=0 when compared to the LE-case, while this difference is less than 3% for β=5 degrees and less than 0.5% for β=15 degrees. The yield load $F_y$ of the YR-case is a better lower bound for $F_{GP}$ of the EBM-case than that of the YLE-case, especially for small β-angles. The difference between $F_{GP}$ of the LE-case and $F_y$ of the YR-case is less than 11% for β=0 when compared to the LE-case, while that difference is less than 20% for β=15 degrees.

The gross plastic failure loads of the EBM-case are also compared with the gross plastic failure loads of a finite element beam model (FEBM-case). The finite element code used herein is NIKE3D (Maker et al., 1991), where nonlinear material and geometric behaviors are considered. The finite element model comprised 100 uniform beam elements. For each beam element, a rectangular cross section having the same area $A(x)$ and second area moment $I(x)$ of the W-section,

calculated at the mid-length of the element, was specified. The material model for each beam element was the elastic perfectly-plastic model implemented in NIKE3D.

For the finite element beam model, the gross plastic failure load was determined by first applying an incremental end displacement $\delta a$ in the desired direction of the end load (quasi-static displacement control). Then, the end load-displacement history corresponding to $\delta a$ was determined. A typical end load-displacement history obtained from the finite element beam model is shown in Fig. 12 for the case of $\beta=0$. As seen, as $\delta a$ increased, the corresponding end load $F$ (FEBM-case) increased (elastic loading curve), peaked, then started to decrease (plastic unloading curve). The point of intersection of the elastic loading curve and the plastic unloading curve (the peak) is the static plastic collapse load of the finite element beam model, $F_{GP}$ of FEBM-case, considering the change of beam geometry during loading. The transition from the elastic loading curve to the plastic unloading curve occured suddenly (not smoothly) since the finite element beam model is still a skeletal presentation of the beam and the spread of the plastic zone is, therefore, neglected. Accordingly, $F_{GP}$ of the FEBM-case is still higher than the true static plastic collapse load of the beam.

Table 1 gives $F_{GP}$ of the EBM-case normalized with respect to $F_{GP}$ of the FEBM-case, for several angles of the end load in the shallow range. As seen, $F_{GP}$ of the EBM-case and $F_{GP}$ of the FEBM-case are in good agreement (within 10%).

TABLE 1 $F_{GP}$ of the EBM-Case Normalized with Respect to $F_{GP}$ of the FEBM-Case

| $\beta$ (degrees) | 0 | 2 | 4 | 6 | 8 | 10 | 12 | 15 |
|---|---|---|---|---|---|---|---|---|
| $\frac{F_{GP}\text{(EBM-case)}}{F_{GP}\text{(FEBM-case)}}$ | 0.97 | 0.97 | 0.97 | 0.96 | 0.96 | 0.94 | 0.93 | 0.93 |

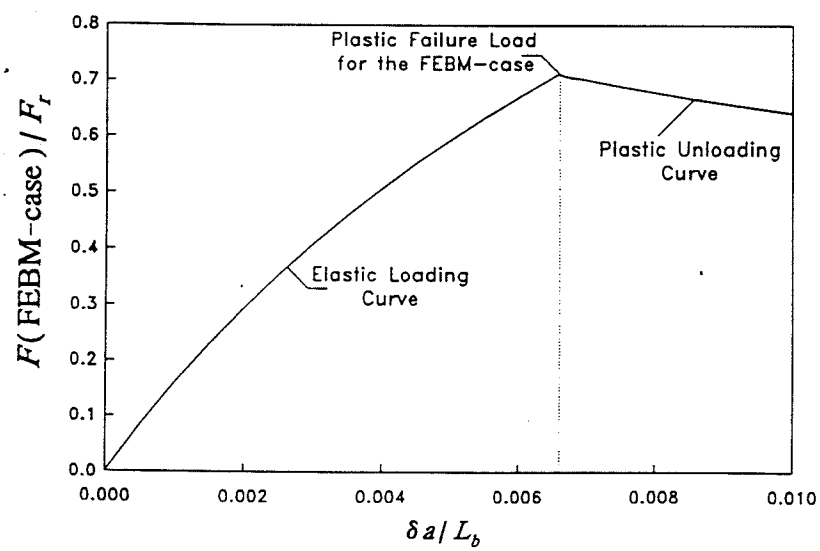


**FIGURE 12 End load-displacement history curves of finite element beam model (FEBM-case) for $\beta=0$.**

## RETROFIT DESIGNS

Retrofit designs A and B are primarily for highway guardrail BCT systems that are installed parallel to the direction of traffic flow, or limited right-of-way straight guardrail BCT systems. A and B were designed considering a head-on vehicle impact, where the angle of the end load $\beta$ vanishes, $\beta=0$. See Fig. 2.

Retrofit design C was developed for highway guardrail BCT systems that are installed with a recommended parabolic curve over the last 37.5 feet with an offset at the end of 4 feet away from the direction of traffic flow (Pigman and Agent, 1988). Design C was developed considering a vehicle impact in a direction parallel to the direction of traffic flow, or $\beta=12$ degrees. This design is effective, however, for all vehicle load angles $\beta$ between 0 and 12 degress

For A, B, and C the initial flat steel sheet used for manufacturing the corrugated section is rectangular. The following design reference parameters of a typical highway guardrail corrugated section are considered: $s_1=9.56$ inches (24.28 cm), $w_1=3.25$ inches (8.26 cm), $h_1=6.125$ inches (15.56 cm), $\alpha_1=0.96$ (55 degrees), $\eta_1=0.059$, $\eta_2=0.094$, $\eta_3=0.313$, $\eta_4=0.254$, and $\eta_5=0.092$. The following reference material characteristics are used: $E=29\times10^6$ psi (200 GN/m$^2$), $\rho=15.22$ slug/ft$^3$ (7853 kg/m$^3$), and $\sigma_y=60{,}000$ psi (414 MN/m$^2$). For the taper profile of the corrugation angle, the following design reference parameters are considered: $q=3$, $r=2$, and $n=2$. Other design reference parameters for A, B, and C are given in Table 2.

In Table 2, the gross plastic failure loads of the retrofit designs $F_{GP}$ were determined such that the expected average vehicle deceleration is below 15$g$ ($g$ is the acceleration due to gravity), which is the maximum recommended occupant ridedown acceleration for the safety of vehicle occupants (Michie, 1981; Ross et al., 1993). The threshold value for the occupant ridedown acceleration is 20$g$. For minicompact and subcompact vehicles that are in the weight range of 1800 to 2500 lb (816 to 1133 kg), the average vehicle deceleration, or the average occupant ridedown acceleration, is expected to be in the range of 5 to 8$g$. It should be noted that A, B, and C were developed considering quasi-static conditions for the application of the end load.

Retrofit design B is initially curved away from the direction of traffic flow more than A, has less gross plastic failure load, and has, therefore, less buckling strength. For both A and B, the taper profile of the corrugation angle was selected to be close to a linear profile ($m=1$). Also, the design load was increased by 10% when compared to the specified gross plastic failure load of the retrofit design, $\phi_F=1.1$, to compensate for the effect of the change of geometry during elastic loading. This effect has been neglected for C since the end load is applied in an oblique manner.

For retrofit design C, the initial transverse tip displacement $d_b$ was determined based on the recommended parabolic curve of the existing guardrail, considering the length of the retrofit design $L_b$. The oblique end-load condition ($\beta=12$ degrees) and the initial curvature of the parabolic flare reduces the buckling strength of the guardrail BCT system. Therefore, a shorter and thicker retrofit design is used so that the performance of C is not largely compromised, especially during impacts involving large passenger vehicles.

## TYPICAL RESULTS AND DISCUSSION

Typical results for retrofit designs A, B, and C are given in Table 3. These results are as follows: the full plastic moment of the corrugated W-section at the expected location for gross plastic failure $M_{FP}$; the reduced plastic moment of the corrugated W-section at the expected location for gross plastic failure $M_{RP}$; the taper ratio $\kappa=I_2/I_1$; the ratio $w_2/w_1$; the ratio $h_2/h_1$; the average shape factor $\nu$ considering bending in the symmetry plane as shown in Fig. 2.2, where $\nu$ is defined as the ratio of the plastic modulus to the elastic section modulus (Horne and Morris, 1982); the upper bound on the lowest

TABLE 2 Design Reference Parameters For Retrofit Designs A, B, and C

| | A | B | C |
|---|---|---|---|
| $L_b$ | 50 inches (1.27 m) | 50 inches (1.27 m) | 45 inches (1.14 m) |
| $d_b$ | 5 inches (12.70 cm) | 10 inches (25.40 cm) | 0.45 inches (1.14 cm) |
| $t$ | 0.1084 inches (2.75 mm) | 0.1084 inches (2.75 mm) | 0.1382 inches (3.51 mm) |
| $F_{GP}$ | 14,500 lb (64,525 N) | 8000 lb (35,600 N) | 12,500 lb (55,625 N) |
| $\beta$ | 0 | 0 | 12 degrees |
| $x_p/L_b$ | 0.35 | 0.40 | 0.30 |
| $\phi_F$ | 1.1 | 1.1 | 1.0 |
| $\alpha_2/\alpha_1$ | 0.4 | 0.3 | 0.4 |
| $m$ | 1 | 1 | 3 |

expected elastic bending frequency $\omega_o^u$ and $f_o^u = \omega_o^u/(2\pi)$; the ratio $\omega_{im}/\omega_o^u$ ($\omega_{im}$ is the expected frequency of impact between errant vehicles and the retrofit designs), where the values shown are for an average impact duration of 100 ms; and the ratio $\omega_{im}/(2\pi\,\omega_o^u)$, which is a measurement of the expected error between the quasi-static and dynamic responses of the retrofit designs (Dally et al., 1984). The upper bound on the lowest expected elastic bending frequencies were calculated using Rayleigh's energy method (Wilson, 1984).

As seen in Table 3, the effect of the normal force is not significant as the difference between $M_{FP}$ and $M_{RP}$ is small (less than 3%). For retrofit design B, $\kappa$ and $w_1/w_2$ are less than those of A and C as $\alpha_2/\alpha_1$ for B is less than that of A and C (see Table 2). For A, B, and C, the corrugation width at the end section is flared around 50% when compared

TABLE 3 Typical Results For Retrofit Designs A, B, and C

| | A | B | C |
|---|---|---|---|
| $M_{FP}$ (lb inch) | 96,388 | 90,844 | 102,117 |
| $M_{RP}$ (lb inch) | 94,747 | 90,373 | 101,500 |
| $\kappa$ | 0.206 | 0.118 | 0.206 |
| $w_2/w_1$ | 0.45 | 0.34 | 0.45 |
| $h_2/h_1$ | 1.47 | 1.51 | 1.47 |
| $\omega_o^u$ (rad/sec) | 383.67 | 380.1 | 416.6 |
| $f_o^u$ (Hz) | 61.1 | 60.5 | 66.3 |
| $\omega_{im}/\omega_o^u$ | 0.164 | 0.165 | 0.151 |
| $\omega_{im}/(2\pi\,\omega_o^u)$ | 0.026 | 0.026 | 0.024 |
| | | | |

with that at the interface section. The profile is almost constant along the length of retrofit designs A, B, and C. This can be a result of having the three retrofit designs tapered such that the ratios $\eta_j$, $j$=1,2,3,4,5, are constant along the length of the retrofit design.

The computed frequencies $\omega_o^u$ for retrofit designs A and B are nearly the same even though B has twice the initial transverse end displacement when compared to A. This is because the effect of the difference between the initial transverse end displacements of A and B is not significant. The assumption of small initial curvatures is considered adequate for design purposes since the initial transverse end displacements are within 20% of the length of the retrofit designs.

For retrofit designs A, B, and C, the results in Table 3 show that the ratio $\omega_{im}/\omega_o^u$<<1 (quasi-static regime for load application), and the expected error between the quasi-static and dynamic responses of the retrofit designs is less than 5%. Accordingly, the assumption that the end load is applied in a quasi-static manner is adequate for design purposes.

The gross plastic failure loads and failure locations for retrofit designs A and C were checked using finite element beam models as discussed earlier, using the aforementioned design reference parameters. For these beam models, the gross plastic failure loads were within 5% of those considered in the design. The gross plastic failure locations for A and C were 35% and 33% of the retrofit length, respectively, away from the interface section. These values agree very well with those considered in the design: 35% and 30% for A and C, respectively, away from the interface section (see Table 2). Three configurations for the beam models of A and C are shown in Figs. 12(a) and (b), respectively (the transverse displacements of the retrofit designs have been magnified compared to the length). These configurations are for the unloaded beam model (C1), the loaded beam model at the occurrence of the plastic hinge (C2), and the loaded beam model well after the occurrence of the plastic hinge (C3).

As angle β of the end load is increased beyond that considered in the design, then the gross plastic failure load of the retrofit design will decrease and the gross plastic failure location will move towards the interfaced end. For retrofit design A, the plastic failure load analysis as well as the numerical results from the program EPFRAME showed that the gross plastic failure location is expected to occur at the interface section for β larger than 2-3 degrees. For retrofit design B, the gross plastic failure location is expected to occur at the interface section for β larger than 5-6 degrees. For β less than 2-3 degrees or 5-6 degrees for A or B, the gross plastic failure locations are expected to develop at sections away from the interface section by 30-40% of the retrofit length. This sudden change in the location of the gross plastic failure location as β increases is a result of the taper profiles of A and B, which are close to a linear profile. Also, the moment due to the end load at the interface section was within 10% of the plastic moment capacity of the corrugated section for both A and B.

## ENGINEERING DRAWINGS: FULL-SCALE AND HALF-SCALE DESIGNS

Engineering drawings for retrofit design B are given in Fig. 13. These drawings were generated using AutoCAD release 12, which is available on the public computer clusters of Duke University. The dimensions shown are meant to be accurate to within 1/32 inches and the angles to within one degree. The direction of the traffic flow is indicated: toward the flaired end. To the left of section A-A, a uniform segment was added to provide for a uniform overlap between the retrofit designs and the existing corrugated section of highway guardrail systems. The details shown for the uniform overlap are those for present-day guardrail terminals of the Department of Transportation of North Carolina. The hole in the valley of the corrugated section and located close to the impacted end is used to bolt the retrofit design to the breakaway post. At the bottom of Fig. 13 are three cross section views. Section C-C, which is located at the one-third the lengthdistance foverall length from the fixed end section A-A, is the expected location of the gross plastic failure. This full-scale design would be made of This terminal would be fabricated from a rectangular sheet of either 10 or 12 gage steel.

Shown in Figs. 14 and 15 are the engineering drawings of two half-scale terminal specimens used in the experimental test program, types I and II. Both types were based on design B of Fig. 13. Shown in Fig. 15 are the cross sections of these test specimens: type I with the one rounded top and type II with the flat top on the outside corrugations. Both have the same flair (side view) and both have the same curvature (plan view).

Shown in Table 4 are the computed results for the gross failure moments $M_{FP}$ and for the upper bounds on the natural frequencies $\omega_o^u$ and $f_o^u$ for both a half-scale version of design A (not used for experiments) and of the type I half-scale design, which was used for the experiments. Note that these characteristics not very different, comparing the two designs.

TABLE 4 Computed Moments and Frequencies for Two Half-Scale Designs

| | Design A | Design B. Type I |
|---|---|---|
| $M_{RP}$ (lb inch) | 24,100 | 22,700 |
| $\omega_o^u$ (rad/sec) | 767 | 760 |
| $f_o^u$ (Hz) | 122 | 121 |
| | | |

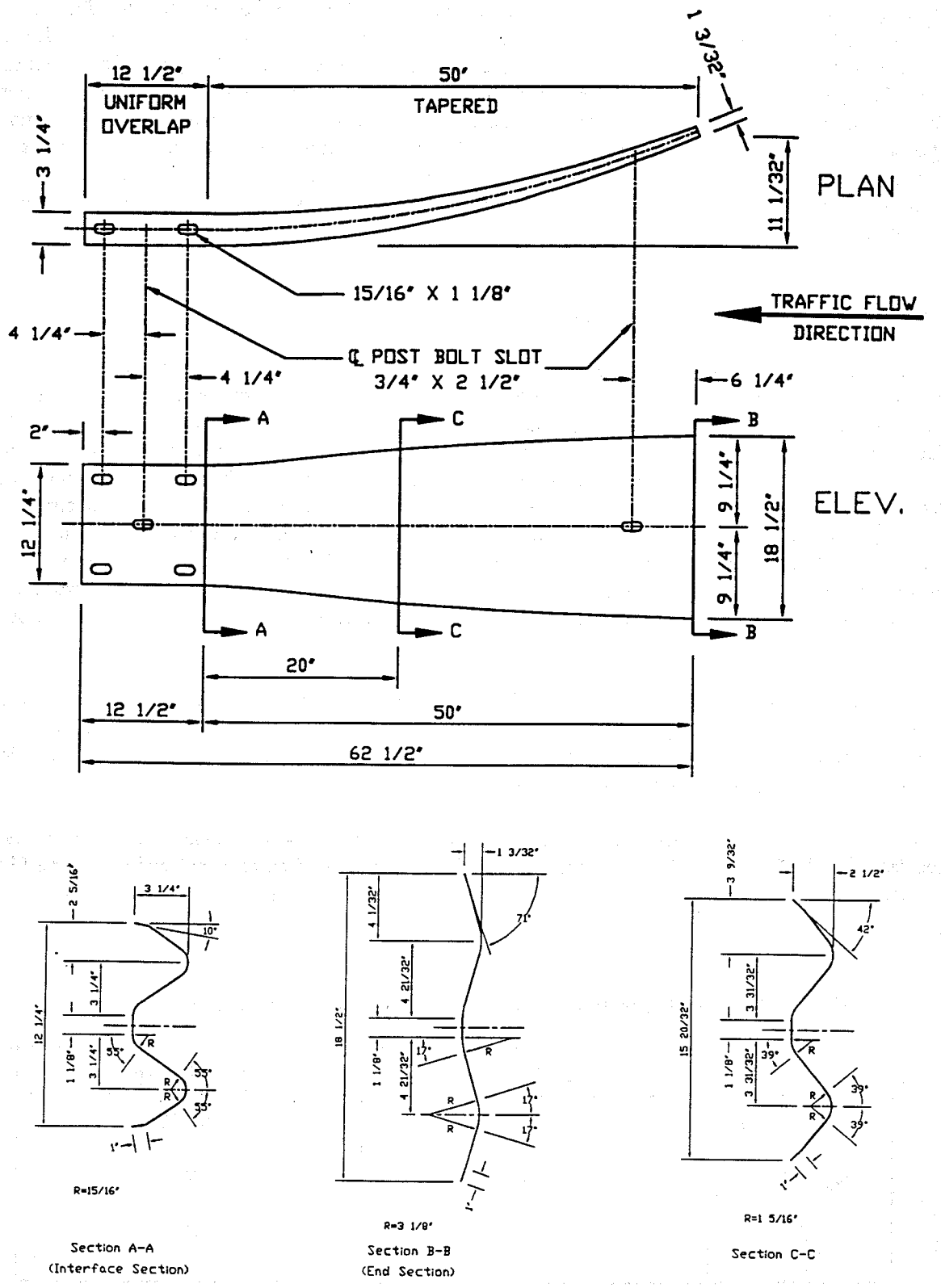


**FIGURE 13 Full scale design B.**

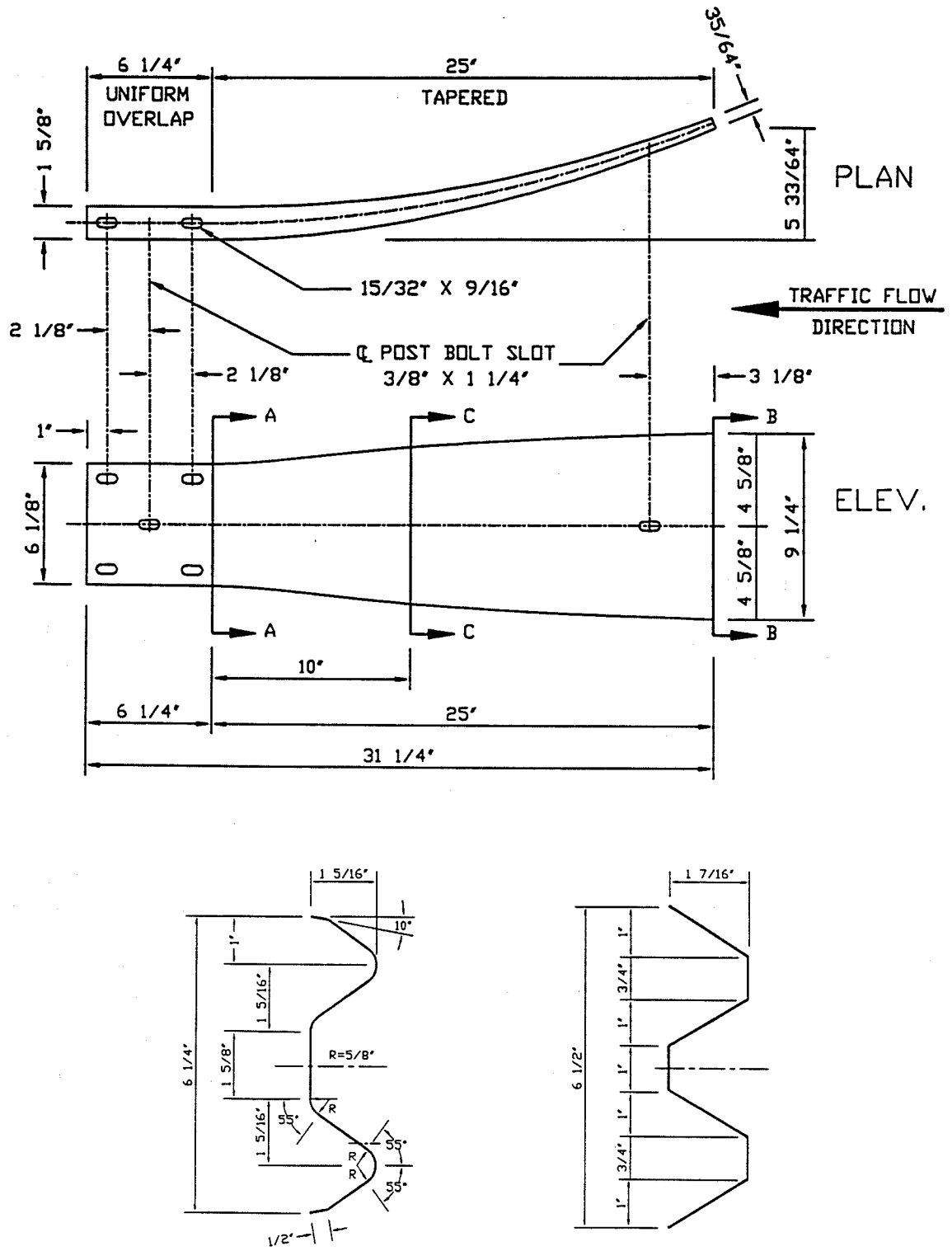


**FIGURE 14** Half-scale design. Sections A-A for type I (lower left) and and for type II (lower right).

## EXPERIMENTS ON THE HALF-SCALE MODELS

Three types of experiments were performed: tensile tests on the 0.072 in. thick, 14 gage steel sheet ( the material of the test models), static buckling tests, and dynamic impact tests. The geometry of the tensile specimens was based on ASTM standards for steel sheet. In all three types of experiments, the specimens were coated with a paint called Stress Coat that showed the onset of material yielding by producing small, visible cracks in the paint.

The results of the two tensile tests are shown in Table 5. The three mechanical properties, Young's modulus, yield stress, and ultimate stress, as well as the initial stress at which cracking of the Stress Coat became visible (at about 47,000 psi) were quite consistant between the two specimens. The flow stress for plastic failure was defined as the average value of the yield stress and the ultimate stress measured in these tensile experiments, or 48,000 psi.

TABLE 5 Mechanical Properties Of The 14 Gage Steel For The Model Terminals

| | Test #1 | Test #2 |
|---|---|---|
| Young's Modulus (psi) | $29.1 \times 10^6$ | $30.5 \times 10^6$ |
| Yield Stress (psi) | $41.3 \times 10^3$ | $41.6 \times 10^3$ |
| Ultimate Stress (psi) | $55.0 \times 10^3$ | $55.1 \times 10^3$ |
| Initial Stress Coat Cracking (psi) | $45.4 \times 10^3$ | $48.6 \times 10^3$ |

Photographs of the two types of specimens used in both the static and inpact experiments are shown in Fig. 15. For economical reasons, these specimens were not die-stamped. Both type I and type II specimens were first formed in a mechanical "break" as straight sections. The corrugations were filled with polyurethane to avoid buckling, when they were next flared in a mechanical press. The curvature was achieved by first sawing transverse cuts every three inches, about half way through the back face (the face away from the road), and then bending the specimen to nearly close up the cuts and thus obtain the desired curvature. The cuts were then carefully filled with a low temperature steel-bronze weld, and polished on the outer face. The welded cuts on the final models are seen in the photographs of Fig. 15.

Photographs for a typical static experiment with the specimen mounted in the universal testing machine and standing alone, are shown in the top photographs of Fig. 16. This is a double specimen configuration symmetric about the middle. The fixed ends were overlapped at the middle and were securely bolted together to simulate the terminal-guardrail connection. The extreme ends were on roller supports. The static loading was applied through the lower roller by the upward motion of the cross head of the universal testing machine. Thus, the loading of the lower roller of this symmetric configuration simulated static vehicle loading.

Observations of the static behavior of specimens types I and II are summarized in Table 6. For type II specimens, the elastic buckling was computed as 2120 lb, which would be nearly the same for type I specimens. In the experiments, however, elastic buckling did not occur. Gross plastic failure occurred at loads much lower than 2120 lb, or at 660 lb for type I and 1000 lb for type II specimens. The main reason that the gross plastic load was only about one-third the predicted value for type I was that premature buckling occurred at the lower roller support. This was avoided in later tests for type II specimens by adding polyurethane inserts at the roller supports, under the corrugations. Thus, type II specimens failed at a higher load of 1000 lb, which was closer to the predicted value of about 1600 lb. There are two

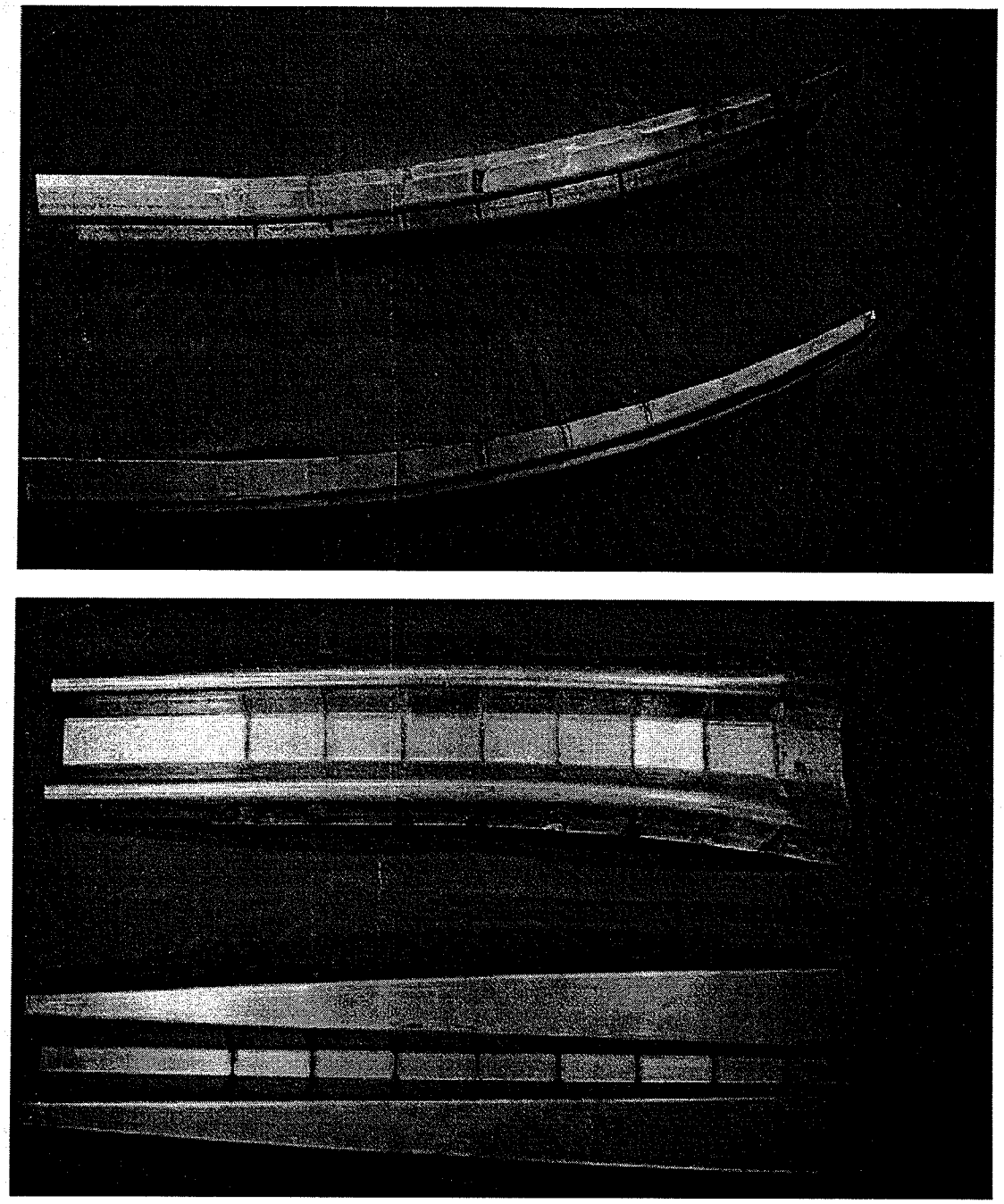

**FIGURE 15 The half-scale models, types I and II: plan views (top) and side views (bottom).**

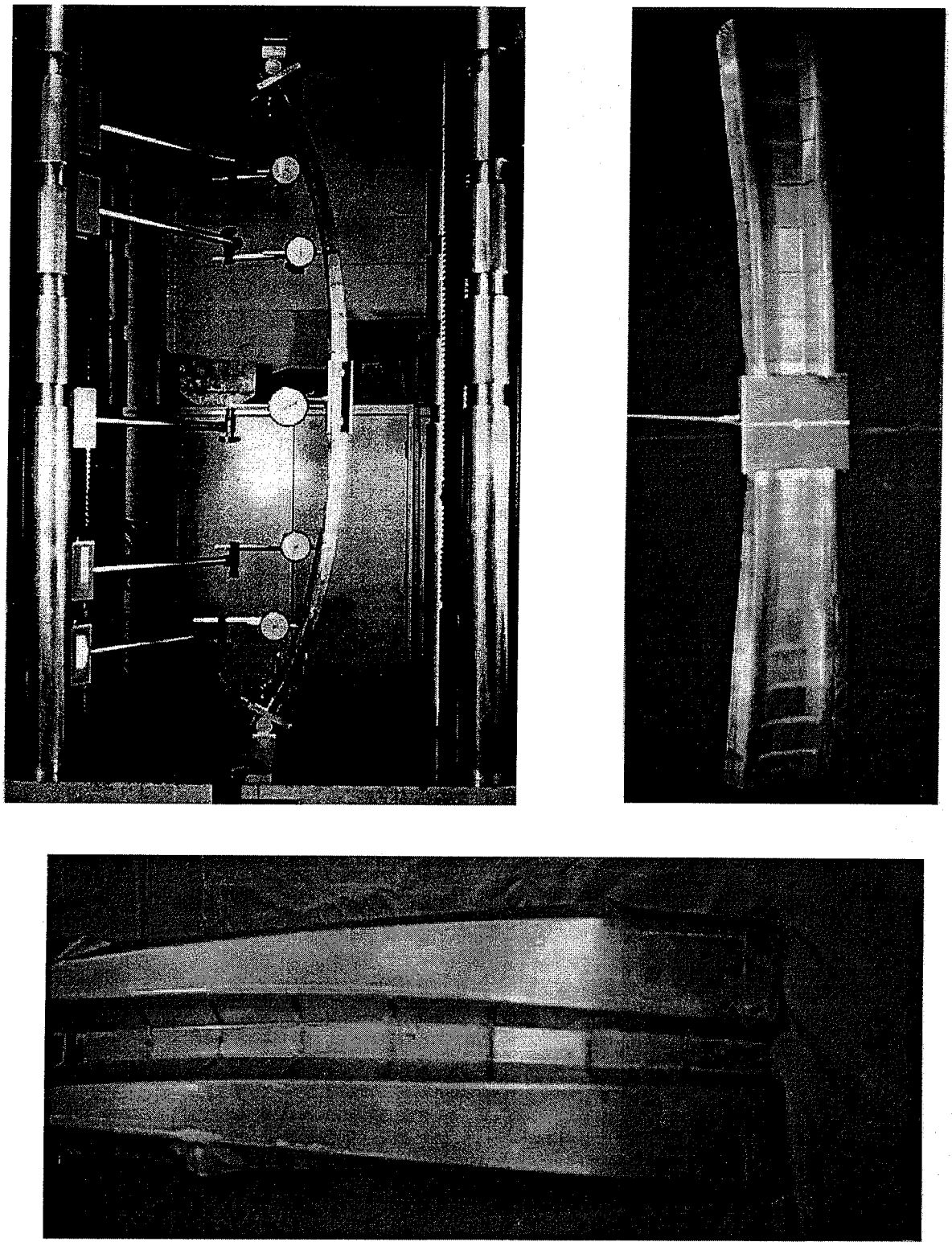

**FIGURE 16 View of a double specimen: edge voew as mounted in the testing machine (upper left); side view (upper right), and a view of a buckled specimen (bottom center).**

main reasons for this latter difference: (1) the actual spread of the plastic zone as failure was approached, observed by the progressive cracking of the Brittle Coat during the experiments, was not accounted for in the analysis; and (2) large changes in geometry during the approach to plastic failure were not included in the analysis. Nevertheless, the analysis did gave a reasonable upper bounds for the gross failure loads. The last and most important observation was that plastic failure did occur at about the third point from the middle (the simulated fixed end), at 10.1 and 7.1 inches whereas the analysis predicted that gross failure would occur at the 10.0 and 10.1 inch points for types I and II specimens, respectively. A photograph of plastic buckling for a type II specimen is shown at the bottom of Fig. 16.

TABLE 6 Static Failure Characteristics of Experimental Models

| | | Specimen type I (rounded-top) | Specimen type II (flat-top) |
|---|---|---|---|
| Elastic Buckling Load (lb) | Analysis | — | 2120 |
| Gross Plastic Failure Load (lb) | Analysis<br>Experiment | 2160<br>650 | 1596<br>1000 |
| Location from Fixed End for Plastic Failure (inches) | Analysis<br>Experiment | 10.0<br>10.1 | 10.3<br>7.1 |

The experimental system for the dynamic impact experiments is shown in the Figs. 17(a) and 17(b). The first of these photographs shows Duke University's test car, a 1984 Honda Accord weighing 2450 lb fully loaded, and fitted with a steel covered wood plank for the front bumper, designed to span the specimen's flare in the vertical plane. The car freely rolled down an incline and its speed just prior to impact was tracked with a videocamera that recorded every 1/30 th of a second the location of the pointer on the bumper along the distance scale on the road. The car's shock absorbers were blocked so that they were not operational. An accelerometer attached to the chassis at midwidth, coupled to its onboard signal conditioner and recorder, was used to measure the ridedown deceleration during impact with terminal specimens.

Before performing the car impact tests on the two specimen configurations, the fundamental free vibration bending frequency was measured for each while clamped in the Y-configuration shown in Fig. 17. The specimen was given a tap transversely with a hammer, and a magnetic-type vibration pickup and recorder were used to measure the transverse vibrations. The measured frequencies were 50 Hz and 31.3 Hz for specimen types I and II, respectively. These were lower than the upper bound frequencies computed from theory (121 Hz for specimen type I, for instance) because the theory assumed full end fixity, whereas the models had only partial end fixity.

The terminal specimens in the Y-configuration, bolted back to the flange of a T-beam, were banded to the steel post serving as the backup. A breakaway post was added near the front flare of each terminal of this Y configuration. See Fig. 17. During impact, which was always somewhat eccentric (the two terminals were never impacted simultaneously), only one of the two buckled plastically, the one that was hit first. The assembly then rotated somewhat around the backup post, and the terminal first hit deformed plastically as shown in the bottom photograph of Fig. 17.

The important results of the dynamic impact experiments are summarized in Table 7. Based on the peak measured ridedown decelerations of 3.1g and 2.6g for the respective specimen configurations I and II, and a car weight of 2450 lb, the corresponding peak failure loads were 7600 lb and 6370 lb. For type II specimens, the average load during impact, which took about 0.1 seconds, was about 1/6 of the peak value, or about 1000 lb, and this agrees with the measured static

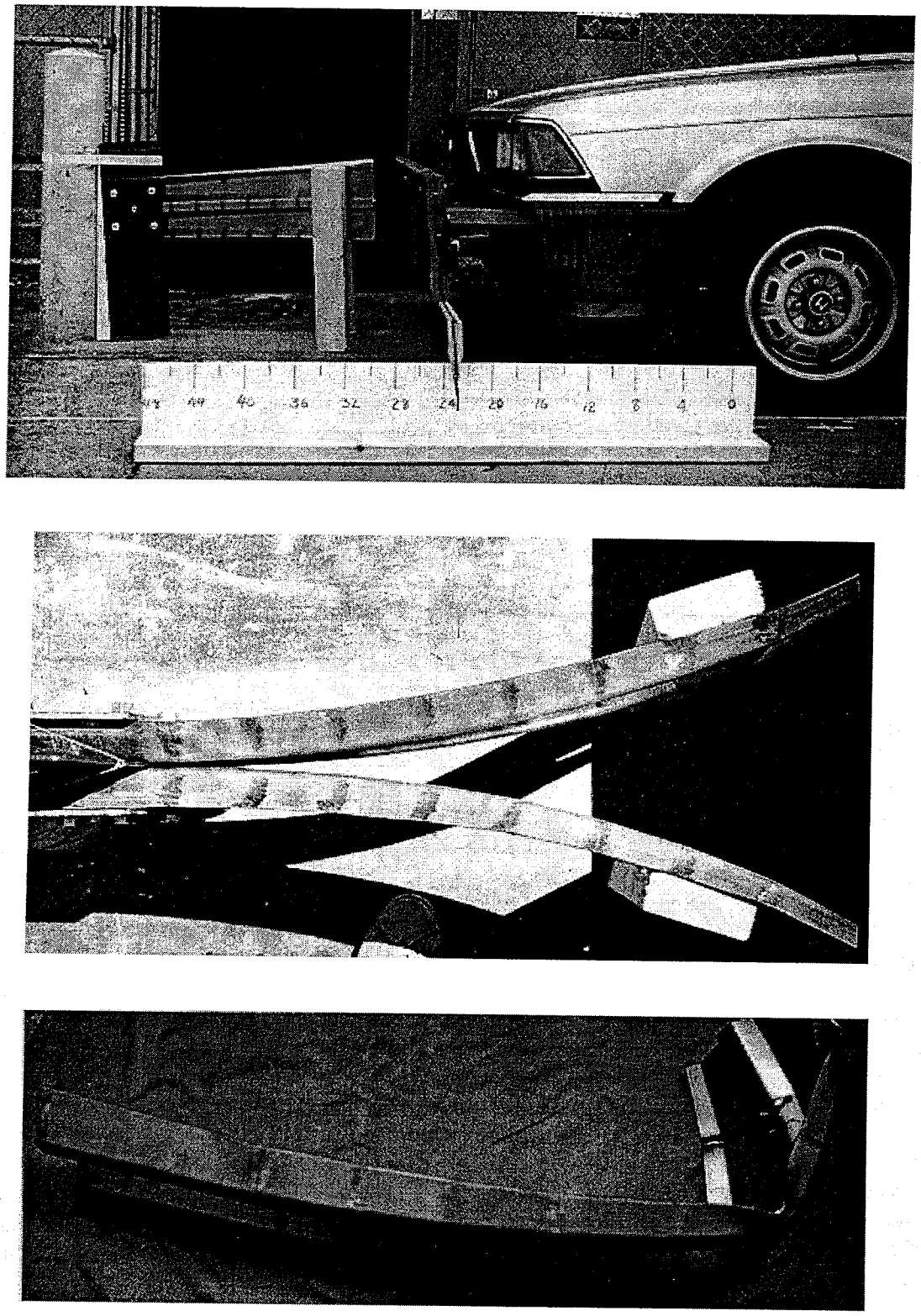

**FIGURE 17 Setup for the dynamic experiments showing the test car and the double specimen configuration (top two photographs) and a typical gross plastic failure mode of a type II specimen (bottom photograph).**

buckling load reported in Table 6. It is noted that type I specimens are stronger than type II specimens, which would be expected since the curved corrugations of I offer more bending stiffness than the flat ones of II.

Most important are the locations of the failure zones for gross plastic failure, which vary from 15 in. to 17 in. from the fixed end for both specimen types. A photograph of a typical dynamic failure of a type II specimen is shown in Fig. 17(c). Whereas the static tests showed plastic failure at 40% of the length from the fixed end, in approximate agreement with static theory, the dynamic tests showed gross plastic failure closer to the loaded end, or at about 64% of the specimen length from the fixed end. These experiments demonstrate that a static analysis may be sufficient for an impacted terminal, although a dynamic theory of gross plastic failure would also be desirable. The important point is that plastic failure occured along the flared length in both static and dynamic experiments, and because of this the buckled terminal then offered a wide frontal area to the impacting car, minimizing the possibility of frontal penetration of the vehicle.

TABLE 7 Dynamic Characteristics of Experimental Models

| | | Type I (rounded-top) | Type II (flat-top) |
|---|---|---|---|
| Measured Peak Load at Failure (lb) | | 7600 | 6370 |
| Measured Location of Gross Buckling (top; center; bottom edges), inches | | 15.4; 17.3; 15.8 | 16.0; 17.5; 15.8 |
| Natural Frequency (Hz) | Theory (upper bound) | 121 | — |
| | Experiment | 50.0 | 31.3 |

## SCALING PARAMETERS: MODEL TO PROTOTYPE

The static test results for type II specimens may be scaled to the full-scale or prototype size provided that the designs remain geometrically similar, or nearly so. Since the type I specimens buckled prematurely at the roller supports, it is recommended that only type II specimens be scaled. For scaling purposes, the dimensionless system parameters defined by equations (16)-(20) should remain invarient, and all of these except equation (18) are automatically invarient if geometric similarity is maintained. For example, the point or region of gross plastic failure will occur at about 40% of the overall length from the fixed end if geometric similarity is maintained. Equation (18), which defines the nondimensional gross failure load, must also remain invarient, and this equation may be used to compute the gross failure load for the prototype whose size,thickness, and yield stress may be different from the model. For example, suppose the half-scale width factor $s_1$ (and therefore the overall geometry except thickness t) increases by a factor of two, the thickness increases by a factor of 1.5, and the yield strength remains the same from the model to the prototype. Then the gross failure load would increase to (2)(1.5)(1000)= 3000 lb for the prototype. It is further hypothesized that the peak dynamic or impact load would also increase by this same factor of three, from 6370 lb measured for the typeII model, to 19,110 lb for the full-scale prototype. This last calculation does need to be varified both by a dynamic analysis and by dynamic impact experiments on full-scale designs.

## CONCLUSIONS AND FUTURE EFFORTS

The three main objectives of this first year study were achieved: (1) to formulate a general static failure theory for a class of new-concept, flared and curved terminals; (2) to use this theory to design guardrail terminals that would not penetrate through vehicles that impacted them; and (3) to test the scale model designs, both statically under laboratory conditions and dynamically with car impact, to show proof of concept. Future work would involve a general formulation of a dynamic impact failure theory for these new-concept terminals. Also, with the cooperation of the North Carolina and the U.S. Departments of Transportation, car crash tests of full-scale terminals with the present design characteristics would be performed. These new terminals would act efficiently when impacted with vehicles of different sizes and coming from both the head-on and the near head-on directions. When implemented, these innovative terminal structures could reduce the present vehicle occupant fatality rate of about 1200 per year attributed to all types of highway barriers.

## REFERENCES


Al-Gahtani, H.J. (1996) Exact stiffnesses for tapered members. *Journal of Structural Engineering* 122(10), 1234-1239.

Dally, J.W., Riley, W.F., and McConnell, K.G. (1984) *Instrumentation for Engineering Measurements*, John Wiley & Sons, Inc., New York.

Dinnik, A. (1932) Design of columns of varying cross-section. *Transactions of Applied Mechanics* 54(APM-54-16), 165-171.

El-Esnawy, N.A. (1997) Analysis and design of tandem vehicles and guardrail breakaway cable terminals for safer highways. *Ph.D. Dissertation*, Department of Civil and Environmental Engineering, Duke University, Durham, North Carolina.

Ermopoulos, J.C. (1986) Buckling of tapered bars under stepped axial loads. *Journal of Structural Engineering* 112(6), 1346-1354.

Horne, M.R. (1979) *Plastic Theory of Structures*, 2nd ed., Pergamon Press, New York.

Horne, M.R., and Morris, L.J. (1982) *Plastic Design of Low-Rise Frames*, MIT Press, Cambridge, Massachusetts.

Karabalis, D.L., and Besko, D.E. (1983) Static, dynamic, and stability analysis of structures composed of tapered beams. *Computers and Structures* 16(6), 731-748.

Lee, H., and Goel, S. (1986) Program EPFRAME: elastic-plastic analysis of plane frames. *Department of Civil and Environmental Engineering*, University of Michigan,
Ann Arbor, MI (unpublished).

Maker, B.N., Ferencz, R.M., and Hallquist, J.O. (1991) *NIKE3D: A Nonlinear, Implicit, Three-Dimensional Finite Element Code for Solid and Structural Mechanics-User's Manual*, University of California, Lawerence Livermore National Laboratory, Rept. UCRL-MA-105268.

Maruthayappan, R., and Lankarani, H.M. (1994) Behavior of structures using simple plastic hinge theory. *Advances in Design Automation (ASME)* DE-69-1, 453-465.

Michie, J.D. (1981) *NCHRP Report 230: Recommended Procedures for the Safety Performance Evaluation of Highway Appurtenances*, TRB, National Research Council, Washington, DC.

Nikravesh, P.E., and Chung, I.S. (1984) Structural collapse and vehicular crash simulation using a plastic hinge technique. *Journal of Structural Mechanics* 12(3), 371-400.

Pigman, J.G., and Agent, K.R. (1988) Performance evaluation of breakaway-cable-terminal end treatments. *Transportation Research Record 1198*, TRB, National Research Council, 1-10.

Ross, Jr., H.E., Sicking, D.L., Zimmer, R.A., and Michie, J.D. (1993) *NCHRP Report 350: Recommended Procedures for the Safety Performance Evaluation of Highway Features*, TRB, National Research Council, Washington, DC.

Siginer, A. (1992) Buckling of columns of variable flexural rigidity. *Journal of Engineering Mechanics* **118**(3), 640-643.

Timoshenko, S.P., and Gere, J.M. (1961) *Theory of Elastic Stability*, McGraw-Hill Book Company, Inc., New York.

Williams, F.W., and Aston, G. (1989) Exact or lower bound tapered column buckling loads. *Journal of Structural Engineering* **115**(5), 1088-1100.

Wilson, J.F. (ed.) (1984) *Dynamics of Offshore Structures*, John Wiley & Sons, Inc., New York.

Wilson, J.F., and Strong, D.J. (1997) Elastic buckling of end-loaded tapered cantilevered beams with initial curvature. *Structural Engineering and Mechanics* 5(3), 257-268.

Wolfram, S. (1993) *Mathematica. A System for Doing Mathematics by Computer*, 2nd ed., Addison-Wesley Publishing Company, Inc., New York.

## APPENDIX I

$$G_1(\alpha_x) = 2\,\eta_2\,\frac{(1-\cos\alpha_x)}{\alpha_x} + \eta_3 \sin\alpha_x \tag{A3.1}$$

$$G_2(\alpha_x) = \frac{\left[(\eta_3 - 2\,\eta_4)\,\eta_5 + 2\,(\eta_3 - \eta_4)\,\eta_4\right]}{4}\sin\alpha_x + \eta_2^2\,\frac{(\sin\alpha_x - \alpha_x)}{\alpha_x^2} + \frac{(8\,\eta_2 + 2\,\eta_3 + 2\,\eta_4 + \eta_5)}{4}\,G_1(\alpha_x) \tag{A3.2}$$

$$
\begin{aligned}
G_3(\alpha_x) = {} & (6\,\eta_3 + 6\,\eta_4 + 1.5\,\eta_5 + 48\,\eta_2)\; G_1^2(\alpha_x) + 96\,\eta_2^2\,\frac{(\sin\alpha_x - \alpha_x)}{\alpha_x^2}\; G_1(\alpha_x) \\
& + \left[12\,(\eta_3 - \eta_4)\,\eta_4 + 3\,(\eta_3 - 2\,\eta_4)\,\eta_5\right]\sin\alpha_x\, G_1(\alpha_x) \\
& + \left[2\,(\eta_3^3 + \eta_4^3) + 6\,(\eta_3 - \eta_4)^2\,\eta_4 + 1.5\,(\eta_3 - 2\,\eta_4)^2\,\eta_5\right]\sin^2\alpha_x \\
& + 36\,\eta_2^3\,\frac{\left[\alpha_x^2 + 0.5\,\alpha_x \sin(2\,\alpha_x) - 2\sin^2\alpha_x + 2\,(\sin\alpha_x - \alpha_x)^2\right]}{\alpha_x^4} \\
& + 2\,\eta_5^3 \sin^2\gamma\,(x) - 24\; G_2^2(\alpha_x)
\end{aligned}
\tag{A3.3}
$$

$$
G_4(\alpha_x) = \eta_2\,\frac{(1 - \cos\alpha_x)}{\alpha_x} + \frac{(4\,\eta_2 + 4\,\eta_3 - 1)}{4}\,\sin\alpha_x
\tag{A3.4}
$$

$$
\begin{aligned}
G_5(\alpha_x) = {} & \frac{\left[(4\,\eta_2 + 4\eta_3 - 1)^2 + 2\,(1 - 4\,\eta_2)^2 + (4\,\eta_2 + 4\,\eta_4 - 1)^2 + 4\,(2\,\eta_4 - \eta_3)\,\eta_5\right]}{32}\sin\alpha_x \\
& + (2\,\eta_2 - 0.25\,\eta_5)\; G_1(\alpha_x) + (1 - 4\,\eta_2 - \eta_3 - \eta_4)\; G_4(\alpha_x) + 3\,\eta_2^2\,\frac{(\sin\alpha_x - \alpha_x)}{\alpha_x^2}
\end{aligned}
\tag{A3.5}
$$